Technical Report No. 22

THE WATCH FORCING DATA 1958-2001: A METEOROLOGICAL FORCING DATASET FOR LAND SURFACE- AND HYDROLOGICAL-MODELS.

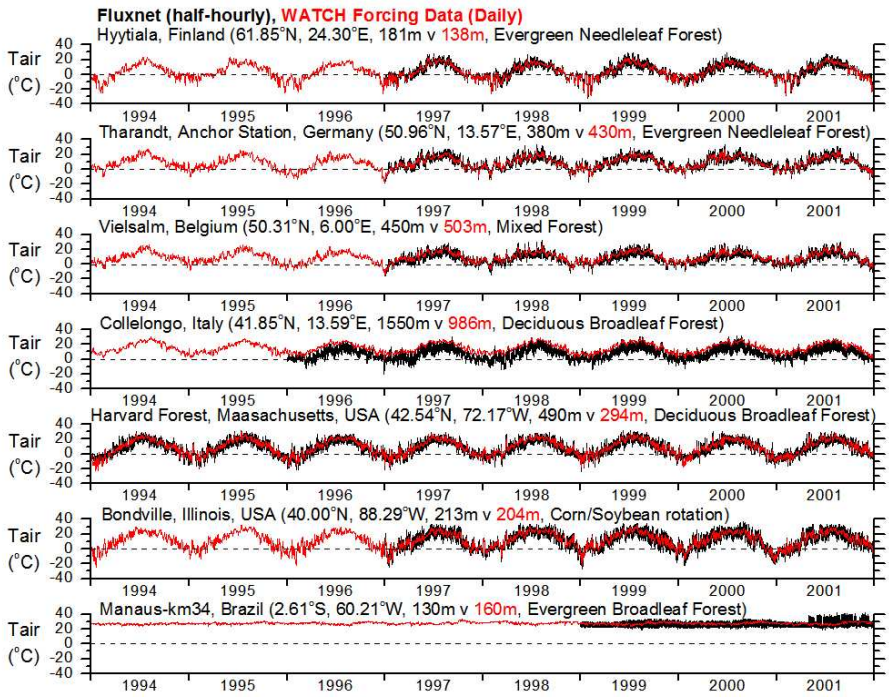

Author names: Weedon, G.P., Gomes, S., Viterbo, P., Österle, H., Adam, J.C., Bellouin, N., Boucher, O., and Best, M.

Date: February 2010

WATCH is an Integrated Project Funded by the European Commission under the Sixth Framework Programme, Global Change and Ecosystems Thematic Priority Area (contract number: 036946).
The WATCH project started 01/02/2007 and will continue for 4 years.

Title:	
Authors:	Weedon, G.P.[1], Gomes, S.[2], Viterbo, P[2]., Österle, H.[3], Adam, J.C.,[4] Bellouin, N.[5], Boucher, O.[5] and Best, M.[1]
Organisations:	1 = Met Office Hadley Centre, Maclean Building, Wallingford, Oxfordshire, OX10 8BB, UK 2 = University of Lisbon, Portugal 3 = PIK Potsdam, Germany 4 = Washington State University, USA 5 = Met Office Hadley Centre, Exeter, UK
Submission date:	February 2010
Function:	e.g. This report is an output from Work Block 1; task 1.1.4
Deliverable	WATCH deliverable 1.1.3

Abstract

New global sub-daily meteorological forcing data are provided for use with land-surface- and hydrological-models. The data are derived from the ERA-40 reanalysis product via sequential interpolation to half-degree resolution, elevation correction and monthly-scale adjustments based on CRU (corrected-temperature, diurnal temperature range, cloud-cover) and GPCC (precipitation) monthly observations combined with new corrections for varying atmospheric aerosol-loading and separate precipitation gauge corrections for rainfall and snowfall.

1) Introduction

In order to investigate the nature of the global water cycle on land within the context of the WATCH EU Programme (www.eu-watch.org), meteorological data are required to be able to run land-surface- and hydrological models. The data described here have been named the WATCH Forcing Data (WFD) and are available in netCDF format following the ALMA convention (web.lmd.jussieu.fr/~polcher/ALMA/) for use by partners and associates via the WATCH ftp site at IIASA, Vienna (ftp://ftp.iiasa.ac.at, - before the end of WATCH this is currently via a username and password). Within Workblock 1 of WATCH the WFD will be used to investigate the hydrological cycle over land during the twentieth century. The data described here cover 1958 to 2001 inclusive; a subsequent technical report will describe the data extended back to 1901.

The WFD are stored at 67,420 half-degree resolution land points only (excluding Antarctica) and, due to storage limitations, provided at 6-hourly time steps for five variables and 3-hourly time steps for three others (Table 1). Code is provided with the data for temporal interpolation of the six-hourly variables to 3-hourly time steps (the interpolation procedure depending on the variable involved as fully commented in the code).

Table 1: Description of the WATCH Forcing Data variables. Data are stored in monthly netCDF files (e.g. Tair_WFD_196206.nc).

Filename prefix	ALMA variable	Variable description	Units	Storage timestep
Tair_WFD_	Tair	2m air temperature (instantaneous)	K	6 hourly
PSurf_WFD_	PSurf	10m surface pressure (instantaneous)	Pa	6 hourly
Qair_WFD_	Qair	2m specific humidity (instantaneous)	kg/kg	6 hourly
Wind_WFD_	Wind	10m wind speed (instantaneous)	m/s	6 hourly
LWdown_WFD_	LWdown	Downwards long-wave radiation flux (average over next 6 hours)	W/m^2	6 hourly
SWdown_WFD_	SWdown	Downwards short-wave radiation flux (average over next 3 hours)	W/m^2	3 hourly
Rainf_WFD_GPCC_	Rainf	Rainfall rate GPCC bias corrected, undercatch corrected (ave. over next 3h)	$kg/m^2/s$	3 hourly
Snowf_WFD_GPCC_	Snowf	Snowfall rate GPCC bias corrected and undercatch-corrected (ave. over next 3h)	$kg/m^2/s$	3 hourly
Rainf_WFD_CRU_	Rainf	Rainfall rate CRU bias corrected and undercatch-corrected (ave. over next 3h)	$kg/m^2/s$	3 hourly
Snowf_WFD_CRU_	Snowf	Snowfall rate CRU bias corrected and undercatch-corrected (ave. over next 3h)	kg/m2/s	3 hourly

These data have been derived from the ERA-40 reanalysis product of the European Centre for Medium Range Weather Forecasting (ECMWF) as described by Uppala et al.

(2005, Table 2). The ERA-40 product includes all the key near-surface meteorological variables required. However, in order to remove model biases (e.g. Betts and Beljaars, 2003; Hagemann et al., 2005), the ERA-40 data require adjustment (here called "bias-correction") based on monthly observational data in the form of the August 2008 version of CRU-TS2.1 from the Climatic Research Unit (University of East Anglia, UK, New et al., 1999; 2000; Mitchell and Jones, 2005).

Table 2: Sources of data used to derive the WATCH Forcing Data

Dataset	Summary	Location
ERA-40	ECMWF reanalysis product	www.ecmwf.int/research/era/do/get/era-40
CRU TS2.1	Climate Research Unit gridded station observations (multiple variables)	www.cru.uea.ac.uk/~timm/grid/CRU_TS_2_1.html
GPCC Full data product v4	Global Precipitation Climatology Centre gridded station precipitation observations	gpcc.dwd.de/ or orias.dwd.de/GPCC/GPCC_Visualiser

Since the CRU observations are available at half-degree spatial resolution it is appropriate to interpolate the one-degree ERA-40 data to the CRU grid prior to the "bias correction". Previous meteorological forcing datasets, notably the NCC data (Ngo-Duc et al. 2005) and the so-called Princeton data (Sheffield et al 2006) were based on interpolating the NCEP-NCAR reanalysis product from two degrees to one degree prior to bias correction that used the CRU TS2.1 data degraded to one degree. Early within the WATCH programme the NCC data were copied directly to the CRU half-degree grid (intentionally without any attempt to interpolate or "elevation correct" or otherwise adjust the values) in order to provide initial forcing data for hydrological modelling including WATERMIP. The CRU half-degree elevations and differences from the ERA-40 one degree grid are illustrated in Fig. 1.

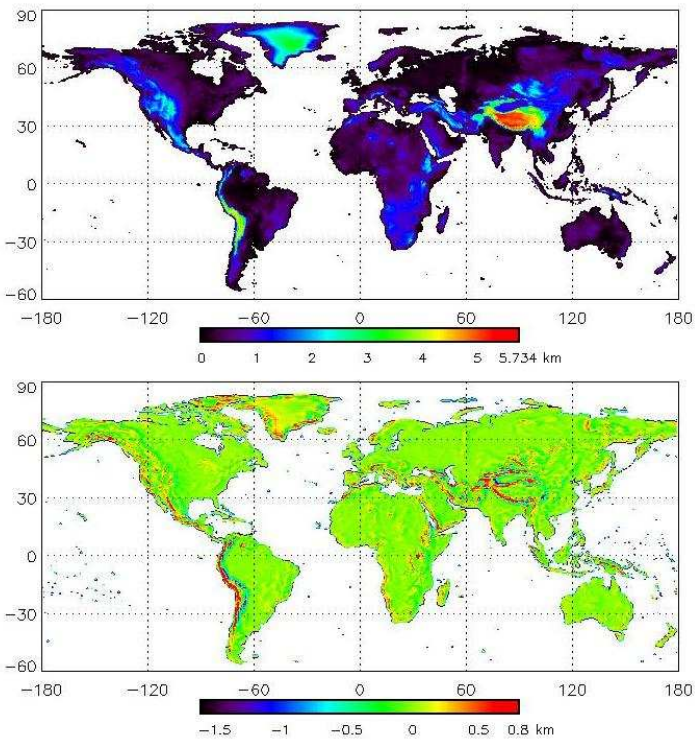

Figure 1: *Top: CRU half-degree elevations and Bottom: differences between ERA (one-degree) and CRU (half-degree) elevations. In this and subsequent figures the numbers on the left and bottom of the map indicate degrees latitude and longitude respectively.*

The key steps in the creation of the WFD for 1958 to 2001, following procedures developed by Ngo-Duc et al (2005) and Sheffield et al. (2006), were therefore: a) bilinear interpolation to the CRU half-degree grid, b) "elevation correction" of certain variables to account for differences in surface heights between the one- and half-degree grids and c) adjustment of certain variables at the monthly scale via the CRU TS2.1 observations. It is critical that the processing of i) 2m temperature, ii) surface pressure, iii) specific humidity and iv) downwards long-wave radiation flux was in that order because the elevation correction using these variables sequentially is required to retain the consistency between variables. Note that only complete years of data have been employed from ERA-40 even though a few months of data at the end of 1957 and the start of 2002 are available. The ERA-40 reanalysis product was derived from general circulation model (GCM) runs that assimilate, via 3D-var, various satellite data, atmospheric soundings and certain land- and sea-surface observations (Uppala et al. 2005). In several respects the ERA-40 product is superior to the earlier NCAR-NCEP reanalysis (e.g. Uppala et al. 2005).

However, despite assimilation of some surface observations, the 2m temperatures in ERA-40 still lack some of the climatic trends and exhibit an overall bias compared to the CRU observations (Betts and Beljaars, 2003; Simmons et al. 2004; Hagemann et al., 2005). Comparison of NCAR-NCEP, ERA-40 and the more recent JMA-25 reanalyses in terms of diurnal extremes in near-surface temperature reveals some problems, particularly in minimum temperatures, in each case (Pitman and Perkins, 2009). Here both the CRU TS2.1 mean 2m temperature and the mean 2m diurnal temperature range (the latter employed by Sheffield et al., 2006, but not Ngo-Duc et al. 2005) were used to improve ERA-40 near surface temperatures at the monthly scale. Despite considerable efforts to improve upon their earlier dataset (Mitchell and Jones, 2005), using methods used to avoid non-homogeneous station data (Peterson and Easterling, 1994; Peterson et al. 1998), the CRU TS2.1 2m temperatures retain a variety of inhomogeneities and outliers (Österle et al. 2003, Brohan et al., 2006). Since 2m temperatures are used both in surface models in their own right and also in the elevation correction of other variables, it was essential to remove these errors during creation of the WFD (discussed in Section 2b).

As well as temperature, CRU observations of monthly average cloud-cover fraction were used in the bias-correction of downwards short-wave radiation fluxes together with the innovation of adjustments for seasonal cycles and decadal-scale variations in aerosol loading (as detailed in Section 2f). In terms of precipitation we corrected the average number of days having precipitation using the CRU number of "wet" days. The total monthly precipitation was corrected using the GPCCv4 full data product (Rudolf and Schneider, 2005; Schneider et al., 2008; Fuchs, 2008) with the CRU monthly totals used to produce alternative rainfall and snowfall products. Monthly precipitation totals were also corrected for gauge "undercatch" (Adam and Lettenmaier, 2003). Note that the HadCRU3 data (Brohan et al. 2006) were not available at half-degree resolution during the creation of the WFD.

The details of the steps used to process the different meteorological variables are discussed in turn below with illustration of some average results plus a comparison of the data for selected years at seven FLUXNET (www.fluxnet.ornl.gov/fluxnet/) sites (i.e. CarbEurope, Ameriflux and LBA sites, Fig. 2 , Persson et al., 2000; Araújo et al., 2002, Suni et al., 2003; Meyers and Hollinger, 2004; Grünwald and Bernhofer, 2007; Urbankski et al., 2007; Göckede et al., 2008). Information about the operation of these sites can be found at www.fluxnet.ornl.gov/fluxnet/siteplan.cfm. When FLUXNET data were missing, for the variables other than rainfall or snowfall, we substituted the average of values from other years

from exactly the same half-hourly or hourly time step. This allowed preservation of local diurnal and annual cycles. However, the precipitation data were not gap-filled. The selection of FLUXNET sites was designed to allow a) direct comparison of data from the early 1990s to 2001 (restricting the geographic availability of such data to, principally, Europe and North America), b) cover a variety of latitudes and climatic regimes, c) cover a variety of land-cover types and elevations. Since the field data are available at half-hourly time steps (hourly for Bondville and Manaus), whereas the ERA-40 data (the basis for the WFD) are 3-hourly, we overlay daily average WFD variables onto the FLUXNET values in the figures in order to illustrate the results of processing the reanalysis data.

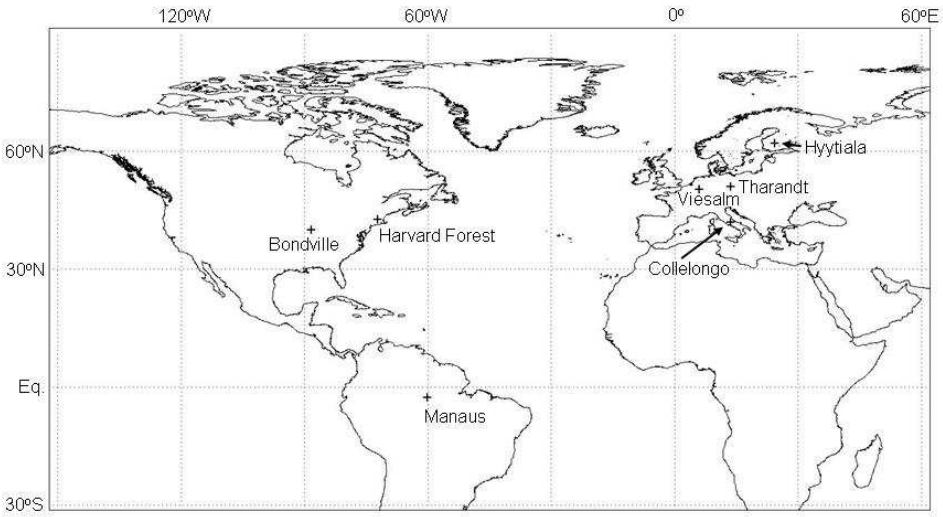

Figure 2: *Locations of Fluxnet sites used in comparison with WATCH Forcing Data.*

2) Creation of the WFD from ERA40 data

2a) Wind speed

Firstly the east-west and north-south wind speed components ERA40 data were squared, added and square rooted to obtain the one-degree wind speed. These data were then bilinearly interpolated from the one-degree ERA land positions (on a two-dimensional, regular longitude-latitude grid, denoted l_{ERA}) to obtain the WFD wind speed at 3-hour time step (t) at each half-degree CRU land point *(l)*:

$$Wind_{WFD}(l,t) = \mathbf{Interp}[Wind_{ERA}(l_{ERA},t)] \quad (1)$$

where **Interp** indicates the operation of bilinear interpolation.

Fig 3 shows half-hourly FLUXNET data (black) compared to daily-average WFD wind speed (red). Naturally the half-hourly FLUXNET data are much more variable than the daily-average WFD wind speeds. Overall the figure demonstrates a good level of agreement. On the other hand, the WFD averages for Bondville appear rather low compared to the FLUXNET site. This probably results from the ERA-40 land cover in the relevant area being

assigned as forest (where slower winds at 10 m would be expected) rather than the cropland of the FLUXNET site.

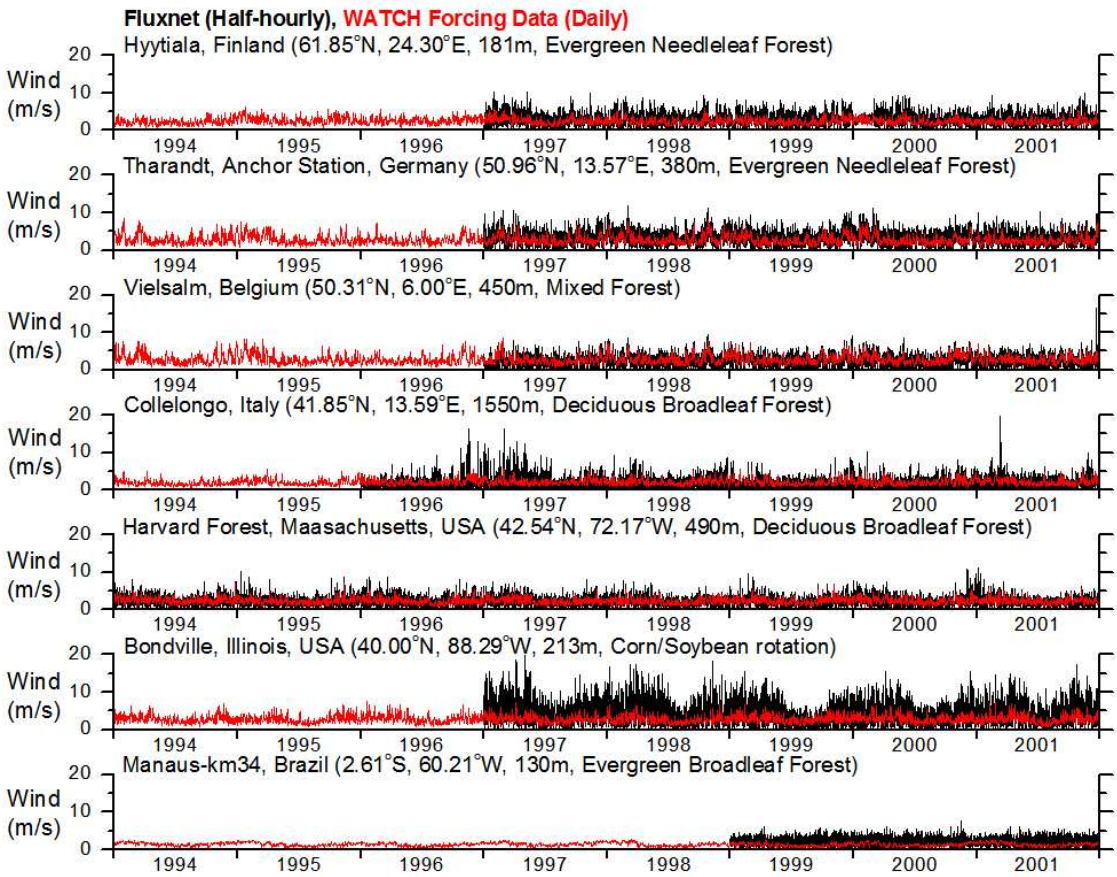

Figure 3: *Comparison of daily average wind speed (Wind) from the WATCH Forcing Data (red) with half-hourly FLUXNET data (black, see fig 2 for Fluxnet site locations).*

2b) 2m temperature

Temperature is a critical variable in the WFD since it is used in the elevation correction of three other variables. In order to obtain 2m temperatures (in K) from the ERA-40 data at half-degree resolution the procedure was to;

a) convert the 2m temperatures at the ERA-40 elevations to 2m temperature at sea-level using an environmental lapse rate of -0.0065 K/m,

b) bilinear interpolate the sea-level 2m temperature to half-degree resolution,

c) convert the interpolated data to 2m temperature at the CRU half-degree elevations. This is represented as:

$$T_{ERA}SL(l_{ERA},t) = T_{ERA}(l_{ERA},t) + (Z_{ERA}(l_{ERA}) \text{ x } 0.0065) \quad (2)$$

$$T_{Interp}SL = \mathbf{Interp}[T_{ERA}SL(l_{ERA},t)] \quad (3)$$

$$T_{Interp}(l,t) = T_{Interp}SL(l,t) - (Z_{CRU}(l) \text{ x } 0.0065) \quad (4)$$

where T_{ERA} and $T_{ERA}SL$ are the ERA-40 2m temperature at the elevation Z_{ERA} (in km) and sea level respectively on the ERA one-degree grid whereas $T_{Interp}SL$ and T_{Interp} are the 2m temperature at sea level and at the elevation Z_{CRU} (in km) respectively, on the CRU half-degree grid.

In order to correct the bias of the ERA-40 surface temperatures (Betts and Beljaars, 2003, Simmons et al. 2004), the monthly average CRU TS2.1 temperatures were used. However, as mentioned earlier the CRU TS2.1 2m temperatures include both multi-year offsets or discontinuities/inhomogeneities, as well as outliers (Österle et al. 2003; Brohan et al. 2006). Extreme examples of both types of error are illustrated in Fig. 4. Such errors appear not to have been corrected by Ngo-Duc et al. (2005) and Sheffield et al. (2006) probably because they used the CRU data degraded to one-degree spatial resolution.

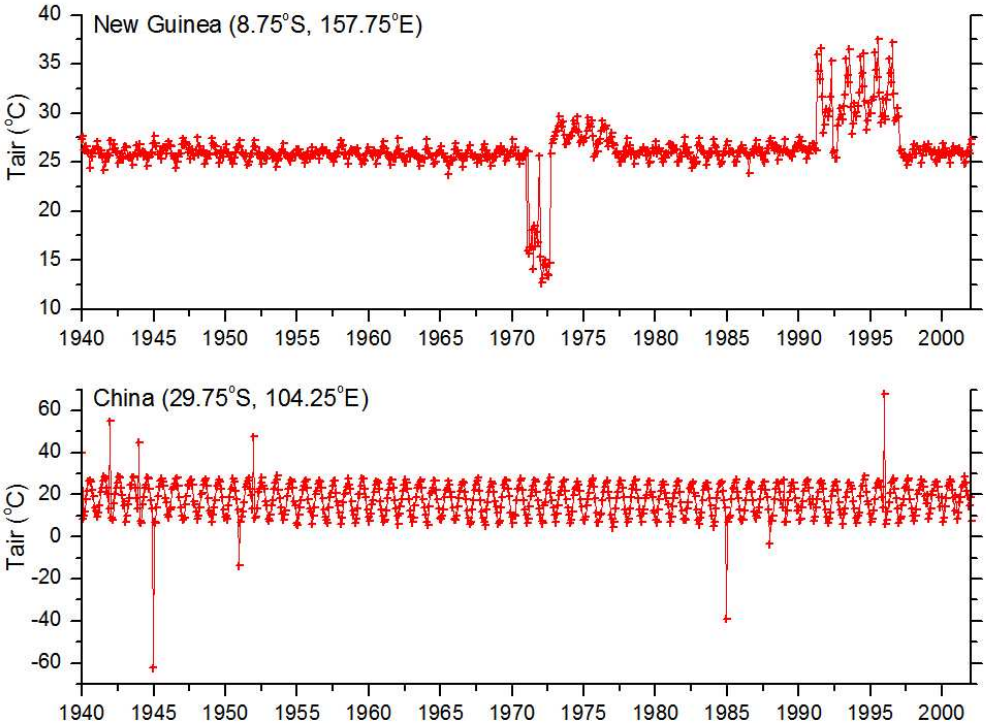

Figure 4 *Top: Example of discontinuities in CRU TS2.1 2m temperature (Tair). Bottom: Example of single month outliers in CRU TS2.1 2m temperature.*

To identify and eliminate the discontinuities in the CRU 2m temperatures we used the procedures of Österle et al (2003) that were originally applied to the first CRU dataset (called CRU-PIK). This involved, at each location, using a 9-year moving window to establish the window mean and standard deviation. At times where a discontinuity caused a statistically significant change in the mean, a replacement mean based on data outside the discontinuity was used to correct the spurious offset (thereby creating CRU-PIK2).

However, this window-based method was unable to identify large single-point outliers (Fig. 4 bottom). To locate the outliers we first calculated, for each grid box, according to the calendar month, the mean and standard deviation of the CRU 2m temperatures (after correction for the multi-month/year discontinuities) from 1958 to 2001. Outliers were then defined as occurring when a particular month had a value more than 5 standard deviations above or below the calendar month average for that grid box. Outlier values were replaced by the calendar month mean. The choice of 5 standard deviations as a threshold for defining outliers represents a somewhat arbitrary attempt to capture extreme spurious values, but yet preserve large natural variability in temperature. Fig. 5 top shows both the maximum difference from 1958 to 2001 at each grid square, between the original CRU data and the

corrected data (up to a maximum of 40 K for 1958-2001 in the Chinese example shown in Fig. 4). The bottom of the same figure shows the number of months (out of 528 for 1958-2001) where the original- and corrected-CRU values differ. Note that most areas and most months are unaffected by the corrections discussed here.

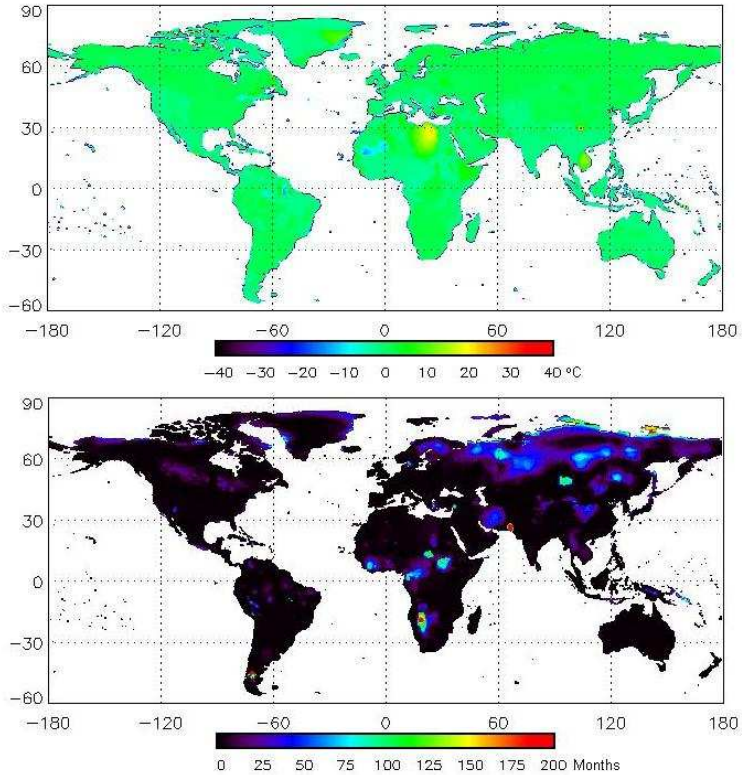

Figure 5 *Top: Maximum differences between monthly average WFD 2m temperature and CRU TS2.1 2m temperature (^{o}C). Bottom: Number of months (out of 528) where WFD and CRU monthly average temperatures differ (due to removal of CRU discontinuities and outliers).*

Once the CRU data had been corrected we applied a "bias-correction" at the monthly scale to the 3-hourly interpolated 2m temperatures using the following equation to obtain the interim temperature (T_{Intm}) from the monthly average interpolated temperature (*TinterpMon*) following Ngo-Duc et al. (2005) and Sheffield et al. (2006):

$$T_{Intm}(l,t) = T_{Interp}(l,t) + T_{CRU}(l,month) - T_{Interp}Mon(l,month) \qquad (5)$$

where T_{CRU} is the (corrected) CRU monthly average temperature with *month* running from January 1958 to December 2001.

Sheffield et al. (2006) also corrected their forcing data using gridded-monthly average diurnal temperatures from the CRU dataset. However, as for the mean-monthly temperatures the diurnal temperature range (DTR) in CRU TS2.1 contains some anomalous January values in this case over northern Greenland (up to 39.8 K). Before correcting DTR we replaced the anomalous January DTR with the averages for the equivalent latitudes outside Greenland (i.e. DTR of around 5 K). The correction takes the form (Sheffield et al. 2006), at each sub-daily time step using both daily- and monthly-averages:

$$T_{WFD}(l,t) = T_{Intm}Day(l,day) + \frac{DTR_{CRU}(l,month)}{DTR_{Intm}Mon(l,month)} \times (T_{Intm}(l,t) - T_{Intm}Day(l,day)) \qquad (6)$$

where $T_{Intm}Day$ is the daily average interim temperature, DTR_{CRU} and $DTR_{Intm}Mon$ are the monthly average diurnal temperature ranges from CRU and T_{Intm} respectively (*day* runs from the first to the last day of the month, *month*) This method preserves the prior monthly average bias-correction of equation 5 (Sheffield et al. 2006).

Fig. 6 compares FLUXNET and WFD 2m temperatures. There is a remarkable level of agreement; the daily average WFD values sit neatly within the range of sub-daily FLUXNET values. This confirms that the WFD 2m temperatures capture the local daily-to-monthly synoptic variability as well as the seasonal (annual) cycle. This result is due to: a) the success of the ERA-40 reanalysis and b) the fact that 2m temperature displays a long "correlation decay distance" (exploited by CRU when gridding meterological station data, New et al., 2000) so that the half-degree WFD derived from the GCM agree very well with the small area sampled by the flux tower data. An exception to this good agreement between WFD and FLUXNET temperatures is exhibited at Collelongo (Italy). The consistently cooler FLUXNET data at Collelongo is simply explained through the environmental lapse rate, because the field site is around 500m higher than the average elevation of the corresponding CRU half-degree grid square.

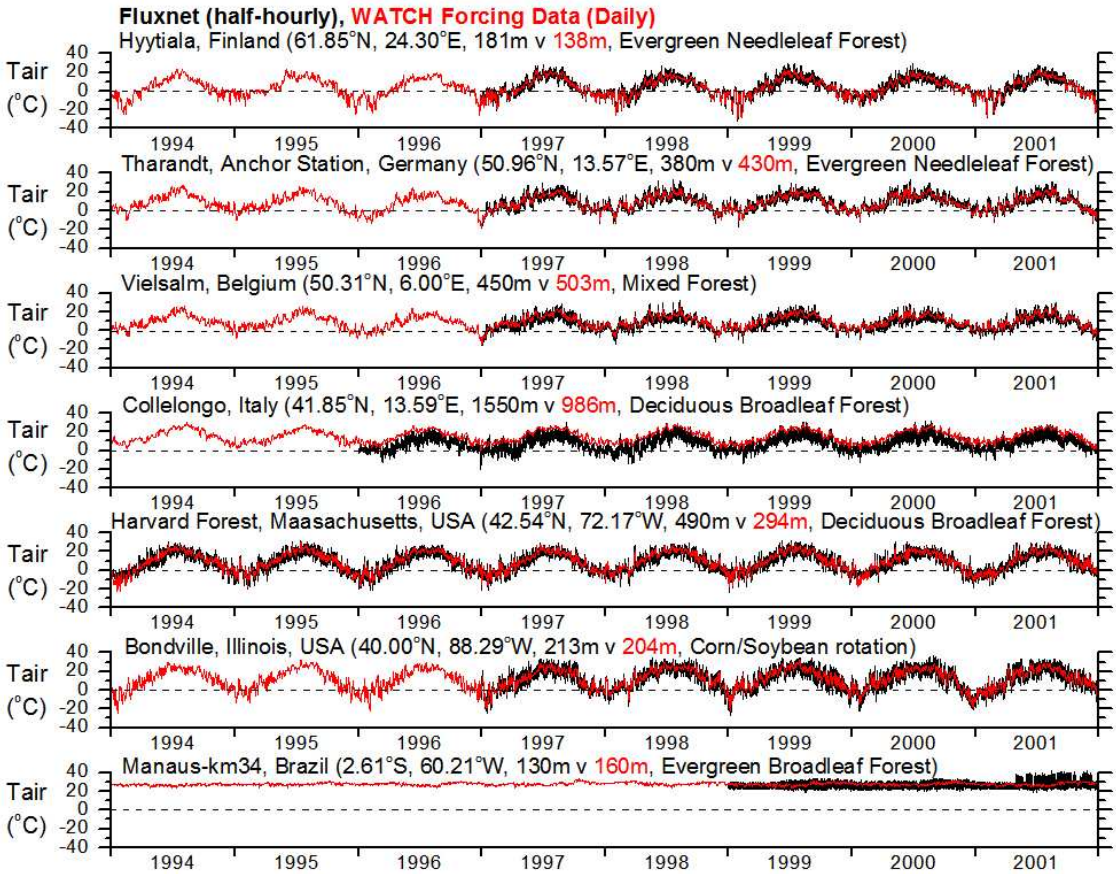

Figure 6: *Comparison of daily average 2m temperature from the WATCH Forcing Data (red) with half-hourly FLUXNET data (black).*

2c) Surface pressure

Aside from the interpolation, the changes to 2m temperatures during bias-correction imply changes to surface (i.e. 10m) pressure. The effects of changes to 2m temperature are

automatically incorporated into surface pressure during the elevation correction needed during bilinear interpolation at sea level. Rearranging equation 2 of Ngo-Duc et al. 2005):

$$PS_{ERA}SL(l_{ERA},t) = \frac{PS_{ERA}(l_{ERA},t)}{(\ T_{ERA}(l_{ERA},t)\ \ /\ (T_{ERA}SL(l_{ERA},t)\ )^{g/-\gamma R}} \tag{7}$$

where g = 9.81 m/s^2, $-\gamma$ = -1.0*environmental lapse rate = 0.0065 K/m and R = gas constant for air = 287 J/kg/K, with PS_{ERA} and $PS_{ERA}SL$ the surface pressure at ERA one-degree elevation and at sea-level respectively (in Pa). Then the bilinearly-interpolated surface pressure at sea level is:

$$PS_{Interp}SL(l,t)\ = \mathbf{Interp}[PS_{ERA}SL(l_{ERA},t)] \tag{8}$$

with, on the half-degree CRU grid:

$$T_{WFD}SL(l,t) = T_{WFD}(l,t) + (Z_{CRU}(l) \text{ x } 0.0065) \tag{9}$$

$$PS_{WFD}(l,t)\ = PS_{Interp}SL(l,t) \text{ x } (T_{WFD}(l,t) / T_{WFD}SL(l,t))^{g/-\gamma R} \tag{10}$$

where $T_{WFD}SL$ is the WFD 2m temperature at sea level and PS_{WFD} is the final surface pressure at the CRU grid elevation.

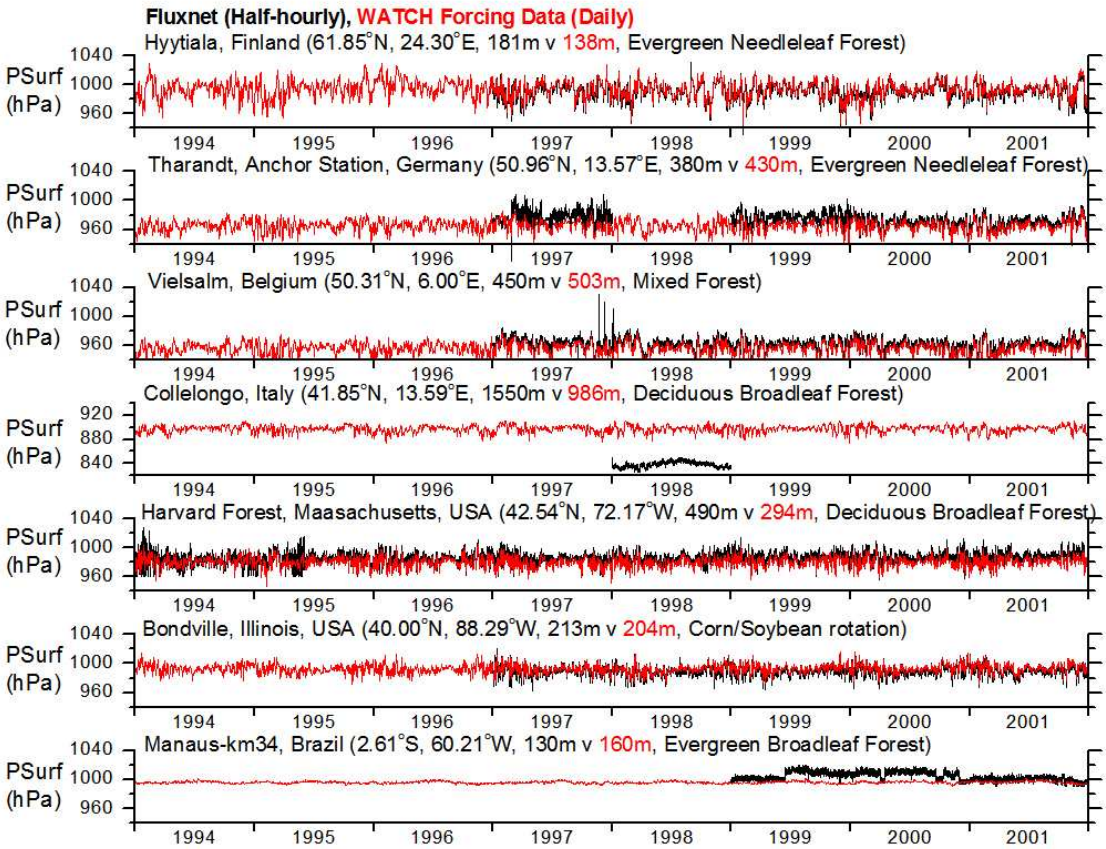

Figure 7: *Comparison of daily average surface pressure (PSurf) from the WATCH Forcing Data (red) with half-hourly FLUXNET data (black).*

The comparison of the WFD surface pressure with FLUXNET data (Fig. 7) shows good agreement aside from: a) the offset in mean pressure at Collelongo that is accounted for

by the difference in elevation between the grid area elevation and the flux tower elevation, and b) apparent problems with flux tower pressure measurements at Manaus in late 1999 and 2000 and at Tharandt in 1997 and 1999.

2d) Specific humidity

Like Sheffield et al. (2006) we followed the methods of Cosgrove et al. (2003) to avoid supersaturation in the WFD that could occur due to elevation changes after interpolation and due to the earlier adjustments to 2m temperature and surface pressure. This required keeping the relative humidity implied by the ERA-40 data fixed during bilinear interpolation at sea level and during elevation correction. Thus firstly saturated water vapour pressure was calculated on the ERA-40 one-degree grid utilizing the 2m temperature in Celcius, TC_{ERA}:

$$TC_{ERA}(l_{ERA},t) = T_{ERA}(l_{ERA},t) - 273.15 \quad (11)$$

Following Willett et al. (2007), the saturated water vapour pressure, $Esat_{ERA}$, was calculated using the equations of Buck (1981) which optimize the Wexler (1976; 1977) equations with specified uncertainty for temperatures between -80° to +50 ^{o}C (193 – 323 K). Initially saturated vapour pressure over water or ice using equation 4a of Buck (1981) is calculated using:

$$Esat_{ERA}(l_{ERA},t) = A \text{ x } \exp [(B - (TC_{ERA}(l_{ERA},t)/D)) \text{ x } TC_{ERA}(l_{ERA},t)) / (TC_{ERA}(l_{ERA},t) + C)] \quad (12)$$

where the constants A to D are obtained from Table 2 of Buck (1981). When TC_{ERA} is above 0.0^o Celcius A = 6.1121, B = 18.729, C = 257.87, D = 227.3. Over ice the values are: A = 6.1115, B = 23.036, C = 279.82, D = 333.7.

The enhancement factor, F_{ERA}, for the saturation vapour pressure, which depends on temperature and surface pressure, is (from equation 6 of Buck, 1981):

$$F_{ERA}(l_{ERA},t) = 1.0 + X + (PS_{ERA}(l_{ERA},t)/100.0) \text{ x } (Y + (Z \text{ x } (TC_{ERA}(l_{ERA},t))^2) \quad (13)$$

with constants X to Z (= A, B and C in Table 3 of Buck (1981). When TC_{ERA} is above freezing: X = 0.00072, Y = 3.2 x10^{-6}, Z = 5.9 x10^{-10}. Over ice: X = 0.00022, Y = 3.83 x10^{-6}, Z = 6.4 x10^{-10}. Applying the enhancement we have:

$$Esat_{ERA}(l_{ERA},t) = Esat_{ERA}(l_{ERA},t) \text{ x } F_{ERA}(l_{ERA},t) \quad (14)$$

The saturated specific humidity, $Qsat_{ERA}$ is then calculated as:

$$Qsat_{ERA}(l_{ERA},t) = \frac{0.62198 \text{ x } Esat_{ERA}(l_{ERA},t)}{(PS_{ERA}(l_{ERA},t)/100.0) - (0.37802 \text{ x } Esat_{ERA}(l_{ERA},t))} \quad (15)$$

and the ERA-40 relative humidity, RH_{ERA} as:

$$RH_{ERA}(l_{ERA},t) = \frac{Qair_{ERA}(l_{ERA},t) \text{ x } 100.0}{Qsat_{ERA}(l_{ERA},t)} \quad (16)$$

with $Qair_{ERA}$ being the specific humidity. Bilinearly interpolated to the CRU half-degree grid the relative humidity becomes:

$$RH(l,t) = \mathbf{Interp}[RH_{ERA}(l_{ERA},t)] \quad (17)$$

Reversing the process to obtain the saturation vapour pressure ($Esat_{WFD}$) on the CRU grid with the WFD pressure and temperature and using:

$$TC_{WFD}(l,t) = T_{WFD}(l,t) - 273.15 \quad (18)$$

we use initially:

$$Esat_{WFD}(l,t) = A \text{ x } \exp[\ (B - (TC_{WFD}(l,t)/D)) \text{ x } TC_{WFD}(l,t)) / (TC_{WFD}(l,t) + C)\ ] \quad (19)$$

and

$$F_{WFD}(l_{WFD},t) = 1.0 + X + (PS_{WFD}(l,t)/100.0) \text{ x } (Y + (Z \text{ x } (TC_{WFD}(l,t))^2) \quad (20)$$

so that:

$$Esat_{WFD}(l,t) = Esat_{WFD}(l,t) \text{ x } F_{WFD}(l,t) \quad (21)$$

Then the saturated specific humidity, $Qsat_{WFD}$, is:

$$Qsat_{WFD}(l,t) = \frac{0.62198 \text{ x } Esat_{WFD}(l,t)}{(PS_{WFD}(l,t)/100.0) - (0.37802 \text{ x } Esat_{WFD}(l,t))} \quad (22)$$

so that finally WFD specific humidity can be calculated using:

$$Qair_{WFD}(l,t) = Qsat_{WFD}(l,t) \text{ x } RH(l,t)/100.0 \quad (23)$$

Fig. 8 shows that this processing has generated daily-average specific humidity values that track the mid-range of half-hourly FLUXNET data. The exception is again Collelongo where elevation differences between the average grid-box height and the flux-tower height have caused an offset (as seen earlier, Fig. 6). Additionally there appears to have been measurement problems in 2001 at Manaus judging by the much increased variability.

The processing (equations 11 to 22) means that the CRU-derived adjustments to mean temperature are consistently incorporated into the WFD specific humidity. This is particularly important since water vapour is a key “Greenhouse gas” so that it is involved in positive climate feedbacks (i.e. rising global temperatures lead to greater global specific humidity if global relative humidity stays constant, Dessler et al., 2008). CRU observations of monthly specific humidity and relative humidity include a climate-change signal attributable to anthropogenic influences (Willett et al., 2007).

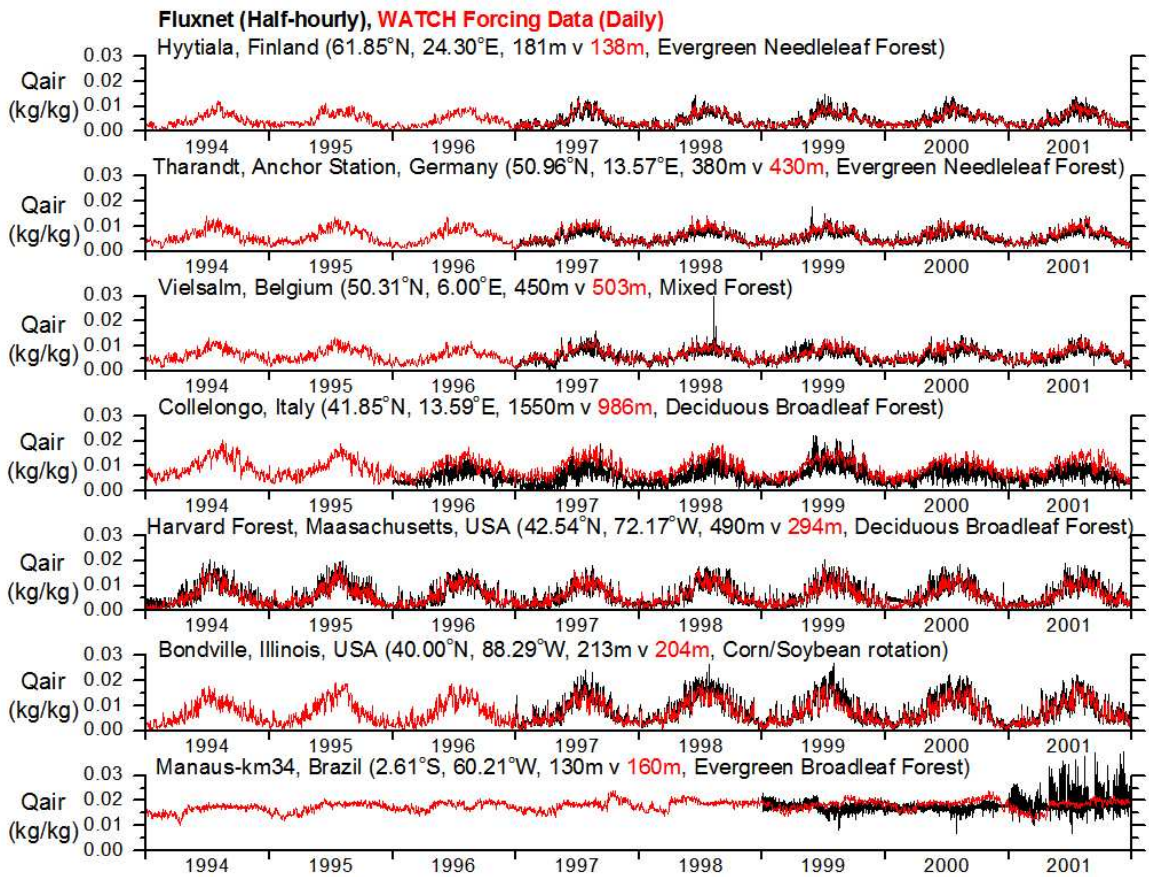

Figure 8: *Comparison of daily average specific humidity (Qair) from the WATCH Forcing Data (red) with half-hourly FLUXNET data (black).*

However, we have not used the monthly CRU TS2.1 vapour pressure values to modify the WFD specific humidity because to do so would compromise the internal consistency of the modified ERA-40 data and potentially lead to spurious supersaturation in some circumstances. Instead we compare the implied vapour pressures with these CRU data. The implied WFD vapour pressure, E_{WFD} is:

$$E_{WFD}(l,t) = \frac{PS_{WFD}(l,t)/100.0 \times Qair_{WFD}(l,t)}{0.62198} \qquad (24)$$

used to compute winter and summer averages (winter = December, January and February or DJF, summer = June, July, August, JJA) for the full dataset. The overall winter average was calculated using December 1959 to February 1960 until December 2000 to February 2001.

Fig. 9a shows the average winter WFD vapour pressure and the difference from CRU Ts2.1 values. The two datasets agree in most places except for higher CRU vapour pressure in parts of the southern Arabian peninisula, Kalahari Desert and parts of central and northern Australia. For summer average vapour pressure, Fig 9b shows that compared to E_{WFD} there are higher CRU vapour pressures in several deserts (Arabian Peninsula, Sahara-, Kalahari-, Gobi- and Mojave-Desert) as well as south-east Brazil, but lower CRU vapour pressures in the Himalayas. A comparison of ERA-40 and CRU dewpoint temperature for 1986-1995 produced very similar patterns of discrepancies (Figure 2 Betts and Beljaars, 2003). All the regions with discrepancies occur where the CRU TS2.1 observations of vapour pressure are

very sparse, especially prior to 1970 (New et al., 1999; 2000; Mitchell and Jones, 2005), so currently it is assumed that in these areas the average WFD vapour pressure is just as likely to be "correct" as the CRU values.

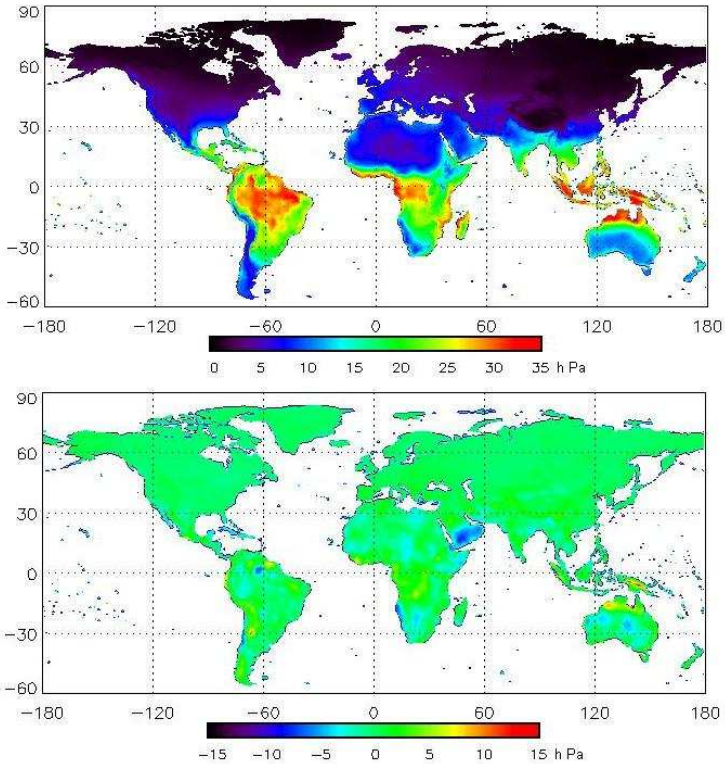

Figure 9a *Top: Average winter (DJF) vapour pressure implied by the WFD specific humidity, 2m temperature and surface pressure (1959-2001). Bottom: Average winter vapour pressure in the WFD minus CRU TS2.1 vapour pressure.*

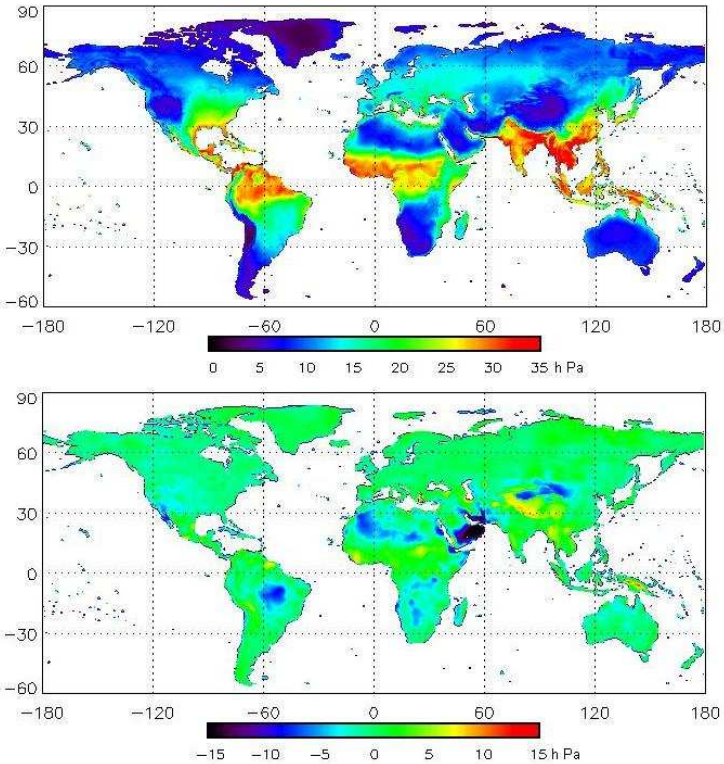

Figure 9b *Top: Average summer (JJA) vapour pressure implied by the WFD (1958-2001). Bottom: Average summer vapour pressure in the WFD minus CRU TS2.1 vapour pressure.*

2e) Downwards long-wave radiation flux

In order to generate the downwards long-wave radiation flux, initially LW_{ERA}, needs to be bilinearly interpolated to the CRU grid. As for Q_{ERA}, LW_{ERA} includes erroneous, slightly negative, values that were replaced by local linear interpolation of adjacent values in time. Interpolation of the corrected ERA-40 values yields, *LWinterp*:

$$LWinterp(l,t) = \mathbf{Interp}[LW_{ERA}(l_{ERA},t)] \quad (25)$$

Following Cosgrove et al. (2003), in order to elevation-correct the interim values it is necessary to copy T_{ERA}, PS_{ERA} and Q_{ERA} (with erroneous values corrected) onto the CRU grid:

$$T_E(l,t) = \mathbf{Copy}[T_{ERA}(l_{ERA},t)] \quad (26)$$

$$PS_E(l,t) = \mathbf{Copy}[PS_{ERA}(l_{ERA},t)] \quad (27)$$

$$Q_E(l,t) = \mathbf{Copy}[Q_{ERA}(l_{ERA},t)] \quad (28)$$

Next vapour pressure, E_E for the copied data was calculated:

$$E_E(l,t) = \frac{PS_E(l,t)/100.0 \text{ x } Qair_E(l,t)}{0.62198} \quad (29)$$

In relation to the Stefan-Boltzmann law for estimating downwards long-wave radiation, the emissivity, ε_E, is calculated using (equation 15 of Cosgrove et al. 2003):

$$\varepsilon_E(l,t) = 1.08 \text{ x } \{1.0 - \exp[-1.0 \text{ x } E_E(l,t)^{TE(l,t)/2016.0}]\} \quad (30)$$

and similarly for WFD values the emissivity, ε_{WFD} is:

$$\varepsilon_{WFD}(l,t) = 1.08 \text{ x } \{1.0 - \exp[-1.0 \text{ x } E_{WFD}(l,t)^{TWFD(l,t)/2016.0}]\} \quad (31)$$

These values allow correction of *LWinterp* via the Stefan-Boltzmann law using (equation 14 of Cosgrove et al. 2003):

$$LW_{WFD}(l,t) = ((\varepsilon_{WFD}(l,t) \text{ x } \sigma)/(\varepsilon_E(l,t) \text{ x } \sigma)) \text{ x } ((T_{WFD}(l,t)/T_E(l,t))^{4.0}) \text{ x } LWinterp(l,t) \quad (32)$$

where σ is the Stefan-Boltzmann constant (5.6704 x10^{-8} W/m^2/K^4).

Fig. 10 compares half-hourly FLUXNET downwards long-wave radiation (black) with monthly average FLUXNET data (grey) and monthly average LW_{WFD} (red). In most places the monthly averages agree very well. However, at Hyytiälä and Harvard Forest the summer FLUXNET data are slightly higher than LW_{WFD}. This suggests either a negative bias in summer LW_{WFD} at these sites or summer bias in the FLUXNET measurements. At Bondville and Collelongo sometimes the FLUXNET monthly averages are higher, sometimes almost identical and sometimes lower than LW_{WFD}.

To interpret these varying offsets we used the NASA downwards long-wave surface radiation budget version 3 (i.e. SRB3 QCLW from eosweb.larc.nasa.gov/PRODOCS/srb/table_srb.html) values to assess bias in LW_{WFD}. Ngo-Duc et al. (2005) and Sheffield et al. (2006) used calendar month averages SRB2 values from

1983-1995 and 1984-1995 respectively to bias-correct their downwards long-wave radiation values. The SRB long-wave values are derived from parameterisation of satellite and meteorological data (Gupta, 1989; Darnell et al., 1992; Gupta et al., 1992). For comparison to LW_{WFD} we follow Ngo-Duc et al. (2005) to find the average calendar month average for 1984-2001, $LW_{SRB}CalMon$, from the bilinearly interpolated one-degree SRB3 QCLW:

$$LW_{SRB}(l,t) = \mathbf{Interp}[LW_{SRB}(l_{SRB},t)] \tag{33}$$

$$LW_{SRB}CalMon(l,calmonth) = \mathbf{Mean}[LW_{SRB}Mon(l,month)] \tag{34}$$

$$LW_{WFD}CalMon(l,calmonth) = \mathbf{Mean}[LW_{WFD}Mon(l,month)] \tag{35}$$

so that the LW_{WFD} can be offset to agree with the long-term average SRB3 QCLW using the 1984-2001 calendar month averages (*calmonth* runs from January to December) via:

$$LW_{WFD}SRB(l,t) = LW_{WFD}(l,t) \times \frac{LW_{SRB}CalMon(l,calmonth)}{LW_{WFD}CalMon(l,calmonth)} \tag{36}$$

applied as an offset for all years (1958-2001).

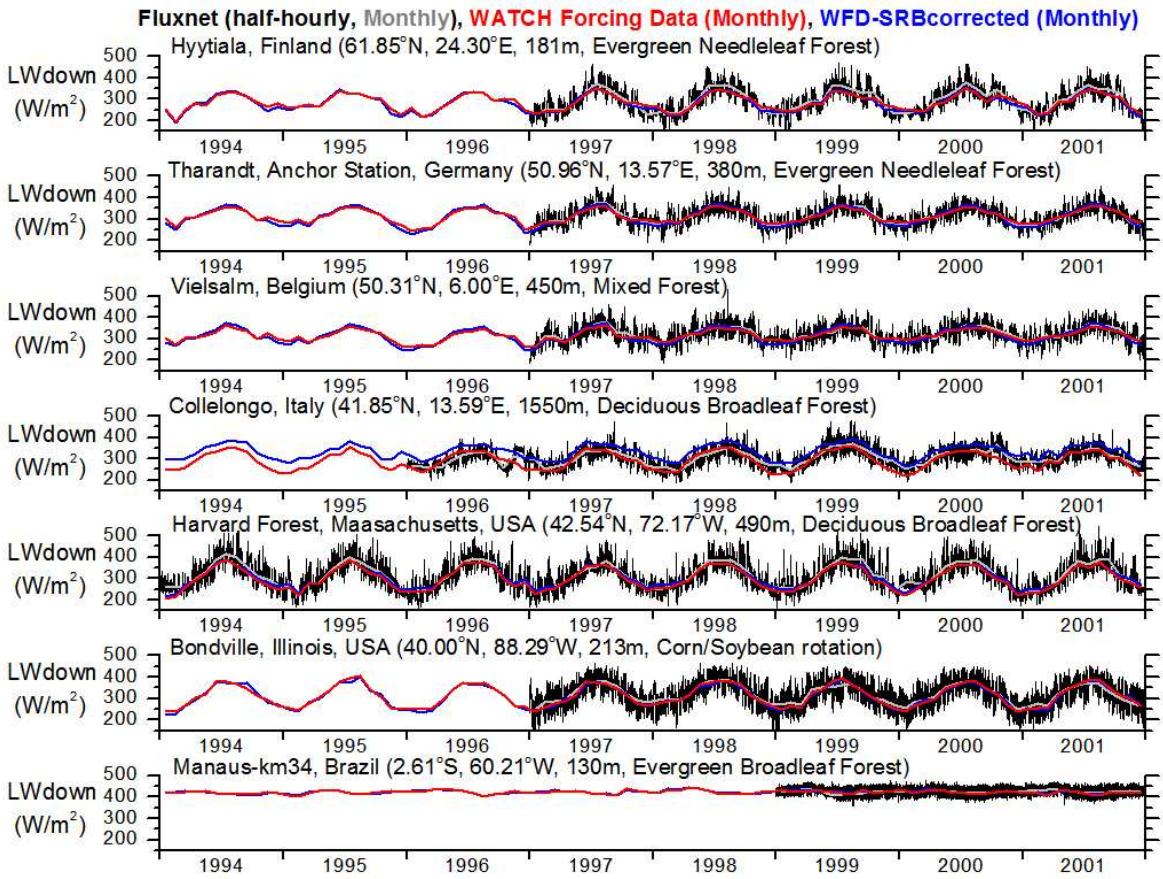

Figure 10: *Comparison of Monthly average incoming long-wave radiation flux (LWdown) from the WATCH Forcing Data (red) with monthly average incoming long-wave radiation flux from SRBv3-corrected WATCH Forcing Data (blue) and with half-hourly (black) and monthly (grey) FLUXNET data.*

Fig 10 shows that the monthly average WFD long-wave fluxes offset using SRB3 (in blue) agree extremely well with the original WFD values at the FLUXNET sites in Europe, North America and Brazil. The exception to this statement applies to Collelongo where the SRB offset leads to values substantially higher than both the WFD values and the FLUXNET values. Nevertheless, this result shows that there is no justification for using an SRB offset to the WFD long-wave data.

Fig 11 illustrates the average winter and summer downwards long-wave in the WFD as well as showing the difference to the SRB-offset results. The LW_{WFD} values show some regions of lower values, especially over mountains (as at Collelongo in Italy) and deserts, compared to the $LW_{WFD}SRB$ values. Gupta et al. (1999) explained difficulties with SRB long-wave fluxes as due to large uncertainties in cloud cover and albedo over deserts and areas covered with snow. Other large regions show that the WFD values are larger than the SRB offset values. The comparison of the original ERA-40 long-wave fluxes with SRB2 data for 1984-1994 by Betts and Beljaars (2003) produced very similar patterns to that found in Fig. 11 (cf. their figure 11). The varying sign of the offset differs substantially from the experience of Sheffield et al. (2006). They found that their NCEP-NCAR derived long-wave fluxes were always elevated compared to SRB offset values worldwide. Hence, unlike this study, they used the offset data as their primary product.

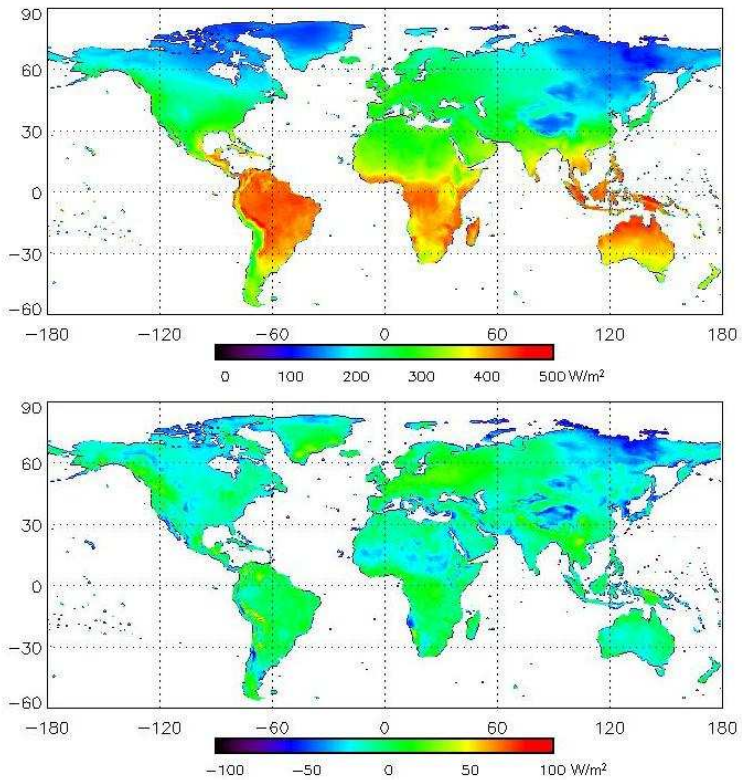

Figure 11a *Top: Average winter (DJF) downwards long-wave radiation flux in the WATCH Forcing Data 1984-2001. Bottom: Average winter downwards long-wave radiation in the WFD minus NASA SRB3-offset WFD 1984-2001.*

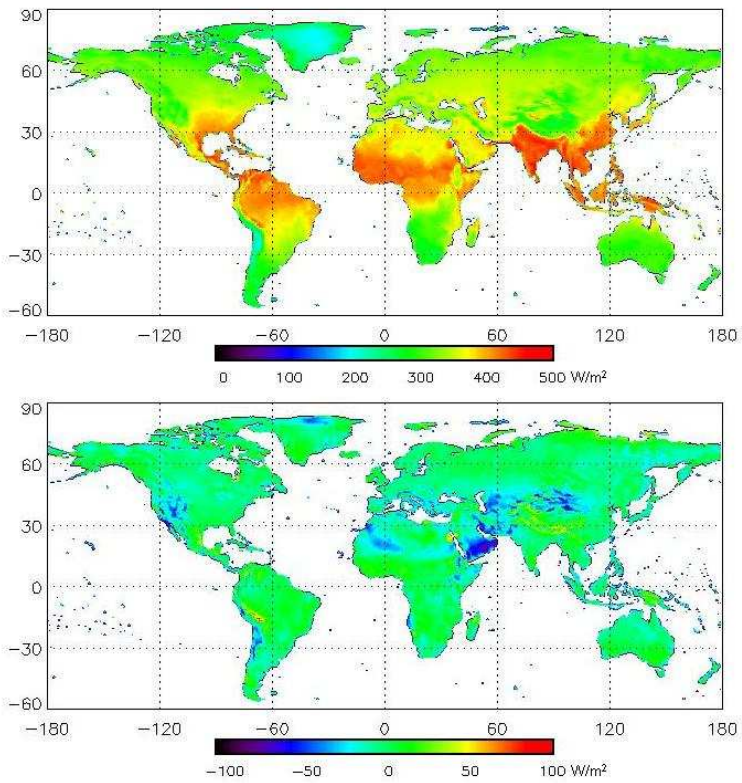

Figure 11b *Top: Average summer (JJA) downwards long-wave radiation flux in the WATCH Forcing Data 1984-2001. Bottom: Average summer downwards long-wave radiation in the WFD minus NASA SRB3-offset WFD 1984-2001.*

2f) Downwards short-wave radiation flux

Bilinear interpolation of the ERA-40 downwards short-wave radiation fluxes, following the re-setting of occasional erroneous slightly negative values (in regions of perpetual darkness throughout the month) to zero, via:

$$SWinterp(l,t) = \mathbf{Interp}[SW_{ERA}(l_{ERA},t)] \quad (37)$$

i) Cloud-cover adjustments

Cloud cover fraction in reanalysis data can differ substantially from observations (Sheffield et al. 2006). Fig. 12 shows time series comparison of monthly average cloud cover fractions in CRU (red) and ERA-40 (grey) at the selected Fluxnet sites. ERA-40 cloud cover agrees with that observed at Tharandt, Vielsalm very well including the mean and variability. However, elsewhere there are important differences, in some cases indicating a seasonal bias (e.g. winter mean offset at Collelongo, winter and summer offsets at Hyytiälä) and in the US and Brazilian sites there are both different means (biases) and different amounts of variability.

Figure 13 shows the winter- and summer-average cloud-cover according to CRU, plus the seasonal averages for ERA-40 minus the CRU seasonal averages. In winter at low latitudes there are many places where the ERA-40 cloud cover is less than the CRU cloud cover. This means that the gridded observations imply more cloud cover than the reanalysis and thus the mean downwards short-wave radiation in ERA-40 is probably too large. At some high latitudes in winter the ERA-40 cloud cover exceeds that according to CRU (Fig. 13a bottom). In summer in most areas where there are large differences, ERA-40 indicates lower

cloud-cover than CRU (implying higher downwards short-wave radiation than the gridded observations would suggest).

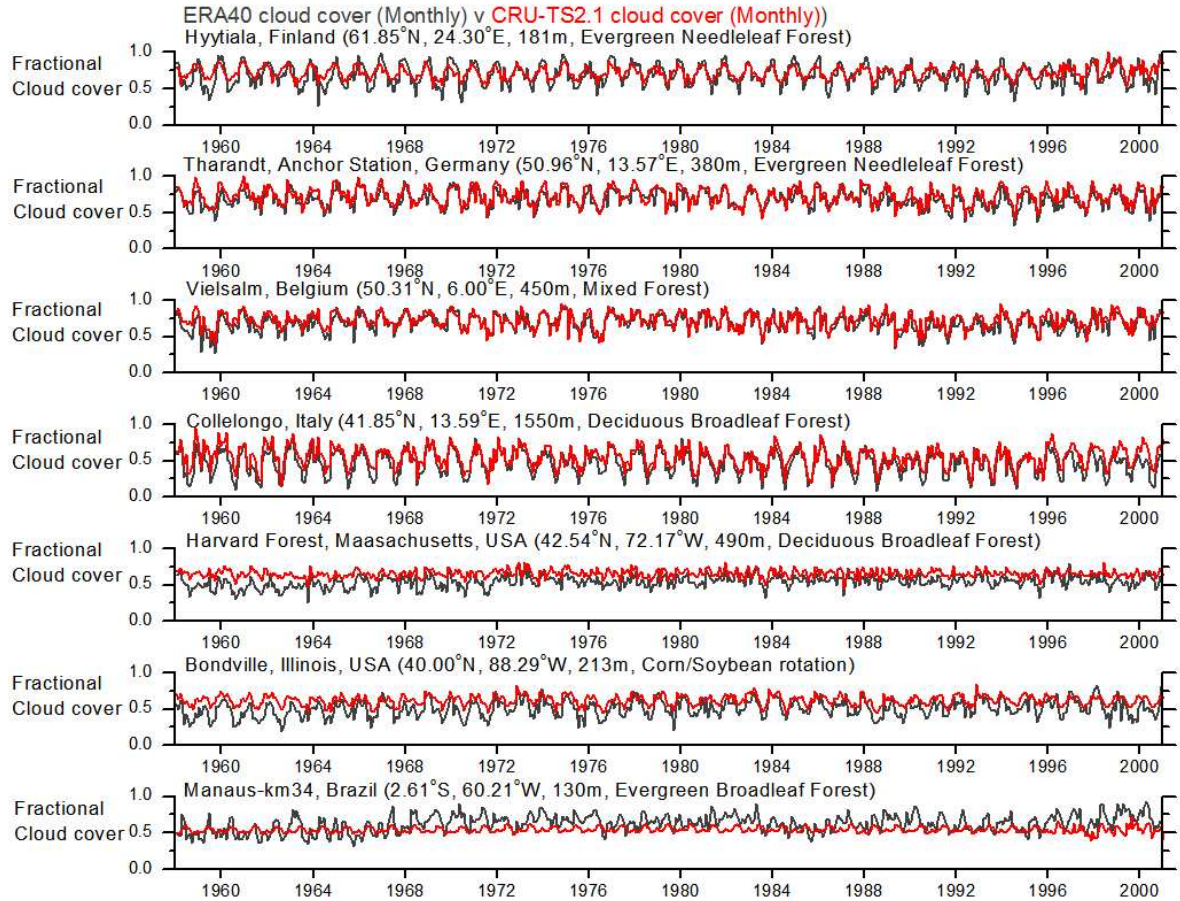

Figure 12: *Comparison of monthly average fractional cloud cover in ERA40 (grey) versus fractional cloud cover in CRU TS2.1 (red) at selected FLUXNET sites for 1958-2001.*

Sheffield et al. (2006) adjusted their interpolated mean monthly short-wave radiation fluxes to be consistent with the CRU cloud-cover fractions. The idea is to use the local relationship between anomalies in monthly short-wave radiation and cloud cover in the interpolated ERA-40 data and then use CRU cloud-cover anomalies to reconstruct the associated short-wave radiation anomalies.

This involved first interpolating the ERA-40 cloud cover fractions and finding the monthly average interpolated ERA-40 downwards short-wave ($SW_{interp}Mon$) and the monthly average interpolated ERA-40 cloud-cover fractions ($Cloud_{ERA}interpMon$). Next the calendar month averages across all years were found using:

$$SWinterpCalMon(l,calmonth) = \mathbf{Mean}[SWinterpMon(l,month)] \quad (38)$$

$$Cloud_{ERA}interp(l,t) = \mathbf{Interp}[Cloud_{ERA}(l_{ERA},t)] \quad (39)$$

$$Cloud_{ERA}CalMon(l,calmonth) = \mathbf{Mean}[Cloud_{ERA}interpMon(l,month)] \quad (40)$$

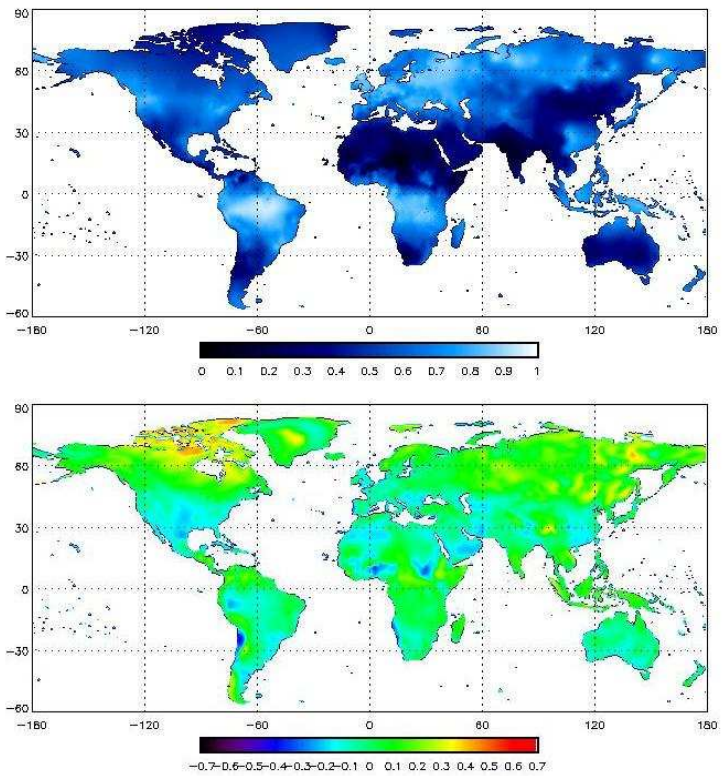

Figure 13a) *Top: Average winter (DJF) monthly cloud-cover fraction according to CRU TS2.1 1958-2001. Bottom: Average winter cloud-cover fraction in ERA-40 minus winter CRU cloud-cover fractions.*

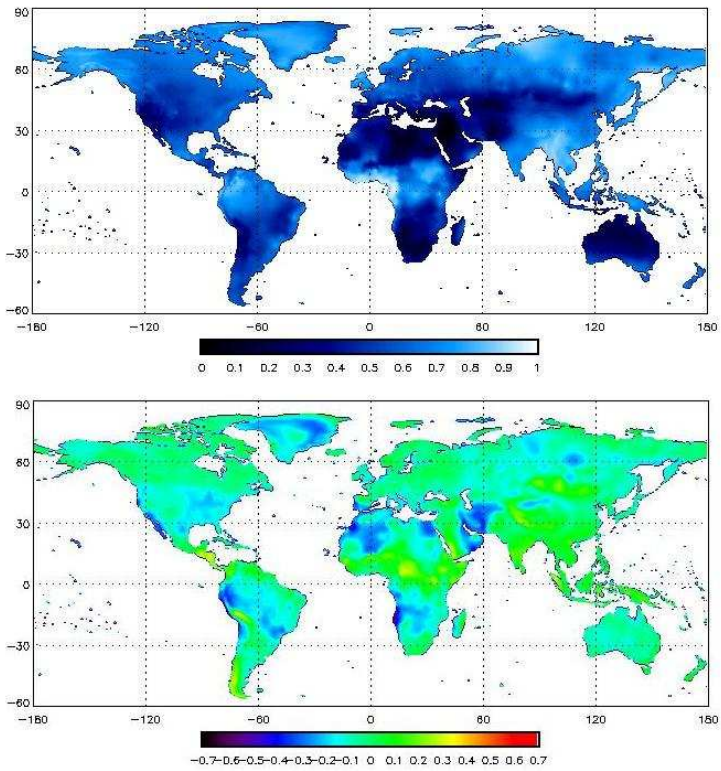

Figure 13b) *Top: Average summer (JJA) monthly cloud-cover fraction according to CRU TS2.1 1958-2001. Bottom: Average summer cloud-cover fraction in ERA-40 minus summer CRU cloud-cover fractions.*

These values were then used to remove the local seasonal cycle yielding monthly anomaly values:

$$Cloud_{ERA}Anom(l,month) = Cloud_{ERA}interpMon(l,month) - Cloud_{ERA}CalMon(l,calmonth) \quad (41)$$

$$SWinterpAnom(l,month) = SWinterpMon(l,month) - SWinterpCalMon(l,calmonth) \quad (42)$$

Generally, decreased monthly cloud-cover fraction is associated with increased downwards short-wave radiation. Thus the linear regression of the cloud-cover anomalies ($Cloud_{ERA}Anom$ = X) versus the short-wave-anomalies ($SW_{ERA}Anom$ = Y) at each location was used to find the local slope (*Slope*) and intercept (*Intercept*) regression parameters. Of course sites that were perpetually dark through the month being processed (at high latitudes in winter) were excluded from the regression and subsequent processing. All regressed sites/months yielded statistically significant correlations between the X and Y values (via the Student's t-test for Pearson's r at the P=0.01 significance level). Using the anomalies in CRU cloud cover ($Cloud_{CRU}Anom$) from:

$$Cloud_{CRU}CalMon(l,calmonth) = \mathbf{Mean}[Cloud_{CRU}(l,month)] \quad (43)$$

and

$$Cloud_{CRU}Anom(l,month) = Cloud_{CRU}(l,month) - Cloud_{CRU}CalMon(l,calmonth) \quad (44)$$

allowed creation of new monthly anomalies in short-wave radiation (*SWnewAnom*) that are expected, given the CRU cloud anomalies (instead of the ERA-40 cloud anomalies), using the local regressions:

$$SWnewAnom(l,month) = Slope(l) \times Cloud_{CRU}Anom(l,month) + Intercept(l) \quad (45)$$

The local *SWinterpCalMon* is then used to recover monthly averages possessing the average seasonal cycle:

$$SWnewMon(l,month) = SWnewAnom(l,month) + SWinterpCalMon(l,calmonth) \quad (46)$$

Finally the sub-daily time step values were adjusted to these new monthly means using an offset. Sheffield et al. (2006) used a ratio method to impose this monthly offset. The ratio offset method is generally preferable to an additive offset (e.g. Equation 5) when the variable in question cannot be negative. Thus:

$$SWintm(l,t) = SWinterp(l,t) \times \frac{SWnewMon(l,month)}{SWinterpMon(l,month)} \quad (47)$$

However, this method proved unsatisfactory in some cases because it created some very unrealistic values. Consider a site where ERA-40 indicates a generally very cloudy month, but with a few clear days. If the monthly adjustment due to the CRU observations implied a rather cloud-free month (large average downwards short-wave flux) the ratio offset method of Sheffield et al. could cause extremely large short-wave fluxes on the few cloud-free days. Consequently, when in a particular location, in a particular month, sub-daily values exceeded the maximum obtained in *SWinterp* at that site for that calendar month across all years, the adjustment for cloud-cover was removed. While not entirely satisfactory, this

safeguard prevents creation of occasional locally unrealistically large short-wave fluxes (e.g. above 500 W/m^2).

ii) Aerosol-loading corrections

There were no adjustments for varying atmospheric aerosol loading in ERA-40 (Uppala et al. 2005). However, long-term changes in aerosol loading can significantly influence downwards short-wave radiation fluxes (e.g. Wild et al., 2008). We have used a correction of downwards short-wave radiation fluxes based on assessing the direct- and indirect-radiative effects of tropospheric- and stratospheric-aerosols on direct- and diffuse-radiation fluxes at the surface. The procedure required assessments of 20th century aerosol optical depths (AOD) from a GCM combined with look-up tables of radiative transfer calculations.

Distributions of tropospheric AOD at 0.55 µm for the 20th century are taken from simulations by the HadGEM2-A GCM which is the atmospheric component of the Hadley Centre Global Environmental Model version 2 (Martin et al., 2006; Collins et al., 2008). HadGEM2-A includes six tropospheric aerosol species: ammonium sulphate, mineral dust, sea-salt, black carbon from fossil-fuel, biomass-burning, and a climatology of secondary organic aerosol from biogenic terpene emissions (Bellouin et al., 2007). When compared with ground-based sun-photometer measurements, the model underestimates the total AOD over Europe and North America in winter and north-western Africa during mineral dust and biomass-burning events. This implies that the corrections used for downwards short-wave radiation are smaller than they should be. On the other hand, simulations are good during summer and throughout the year in Asia, southern Africa, and South America (Bellouin et al., 2007).

Changes in AOD throughout the 20th century were obtained by varying emissions of aerosols and their precursors. Distributions of tropospheric AOD for the six aerosol types are provided from the GCM at a resolution of 1.25º latitude by 1.875º longitude (indicated below using the indexing: l_{GCM}) as monthly means every ten years from 1900 to 1980, and every five years from 1980 to 2000. Monthly distributions for years not simulated are obtained by linearly interpolating the modelled distributions. 20th-century distributions of stratospheric aerosols from volcanic eruptions are provided as zonal means by Sato et al. (1993, dataset updated in 2002).

Aerosol radiative effects are split into the direct effect in the clear-sky (cloud-free) part of a grid box and indirect effects in the cloudy-sky part. Hereafter, the shortwave spectrum covers wavelengths from 0.28 to 4 µm.

In clear-sky, the aerosol direct effect at the surface is the difference between radiative fluxes computed using the AOD distributions described above and fluxes computed with an AOD of zero. Downward direct- and diffuse-radiative fluxes depend on the solar zenith angle, type and optical depth of the tropospheric aerosol, and optical depth of the stratospheric aerosol. Aerosol phase function and scattering and absorption coefficients are computed for all aerosol species at 24 wavelengths using Mie calculations. Size-distributions and refractive indices are those used in HadGEM2-A (Bellouin *et al.*, 2007), except for mineral dust (Dubovik et al., 2002) and stratospheric aerosols (Myhre et al., 2004). The computed aerosol optical properties are used in the discrete-ordinate solver *Streamer* (Key, 1998). This radiative transfer code is used with 24 bands in the shortwave spectrum and 24 streams. Aerosol phase functions are decomposed into their first 48 Legendre moments. Tropospheric aerosols are

assumed to be homogeneously distributed across the lowest kilometre of the atmosphere, while stratospheric aerosols reside in a homogeneous layer between 15 and 20 km. Calculations account for only one tropospheric aerosol species in combination with the stratospheric aerosol. Ocean surface albedo is computed using Cox and Munk (1954). Land surface albedo is that of a generic, green vegetation, obtained by averaging the reflectance of grass, dry grass, and deciduous and coniferous forests. It should be noted that the surface albedo has only a second-order effect on downward fluxes. A standard mid-latitude summer profile is used for gaseous absorption, and Rayleigh scattering is included. When building look-up tables, the cosine of the solar zenith angle is varied from 0.1 to 1.0. The tropospheric and stratospheric AOD are varied from 0 to 2.5 and 0.5, respectively. For all quantities, the step of the variation is 0.05.

In cloudy sky, the aerosol direct effect is assumed to be zero: its signal is masked by the extinction of clouds. There remains the estimation of aerosol indirect effects on clouds. The CRU time series only characterise clouds by their fractional cover, which does little to determine shortwave fluxes. Cloud type and optical thickness are unknown and surface fluxes cannot be computed similarly to the clear-sky case. As an alternative, scaling factors between the aerosol direct effect in clear-sky and indirect effects in cloudy-sky are derived from the HadGEM2-A simulations used to obtain the AOD distributions. In those simulations, sulphate, sea-salt, biomass-burning, and secondary organic aerosols exert indirect effects on large-scale and shallow convective liquid clouds. Scaling factors are computed for each season and for 15 regions of the world.

The clear-sky direct effect in a given grid-box at a given time and date is obtained from the look-up table record corresponding to the current solar zenith angle, and tropospheric and stratospheric optical depths. Since look-up tables do not include combinations of different tropospheric aerosol types, the whole tropospheric column is assumed to have the optical properties of the dominant aerosol. Look-up table fluxes are linearly interpolated in solar zenith angle and tropospheric AOD. The cloudy-sky indirect effect is given as the clear-sky direct effect multiplied by the regional and seasonal scaling factor, except for gridboxes where mineral dust is the dominant aerosol species, as mineral dust does not exert an indirect effect on liquid clouds.

Summarizing the corrections calculated on the GCM grid provide a) correction for clear-sky downwards radiation accounting for the direct effect and indirect effect of aerosols in the troposphere plus the direct effect in the stratosphere (*sdre*) and b) correction for cloudy-sky downwards radiation in the troposphere (*ire*). Note that it is assumed that stratospheric aerosols do not influence cloudy-sky radiation fluxes because they do not interact with tropospheric clouds. Aerosol indirect effects on tropospheric and stratospheric ice clouds are not accounted for, as aerosol impacts on ice cloud nucleation remain uncertain. The correction terms were interpolated to the CRU grid:

$$sdre(l,month) = \mathbf{Interp}(sdre(l_{GCM},month) \quad (48)$$

$$ire(l,month) = \mathbf{Interp}(ire(l_{GCM},month)) \quad (49)$$

and combined with CRU cloud-cover fractions via:

$$SWcorr(l,month) = (sdre(l,month)\text{x}(1\text{-}Cloud_{CRU}(l,month)) + (ire(l,month)\text{x}Cloud_{CRU}(l,month)) \quad (50)$$

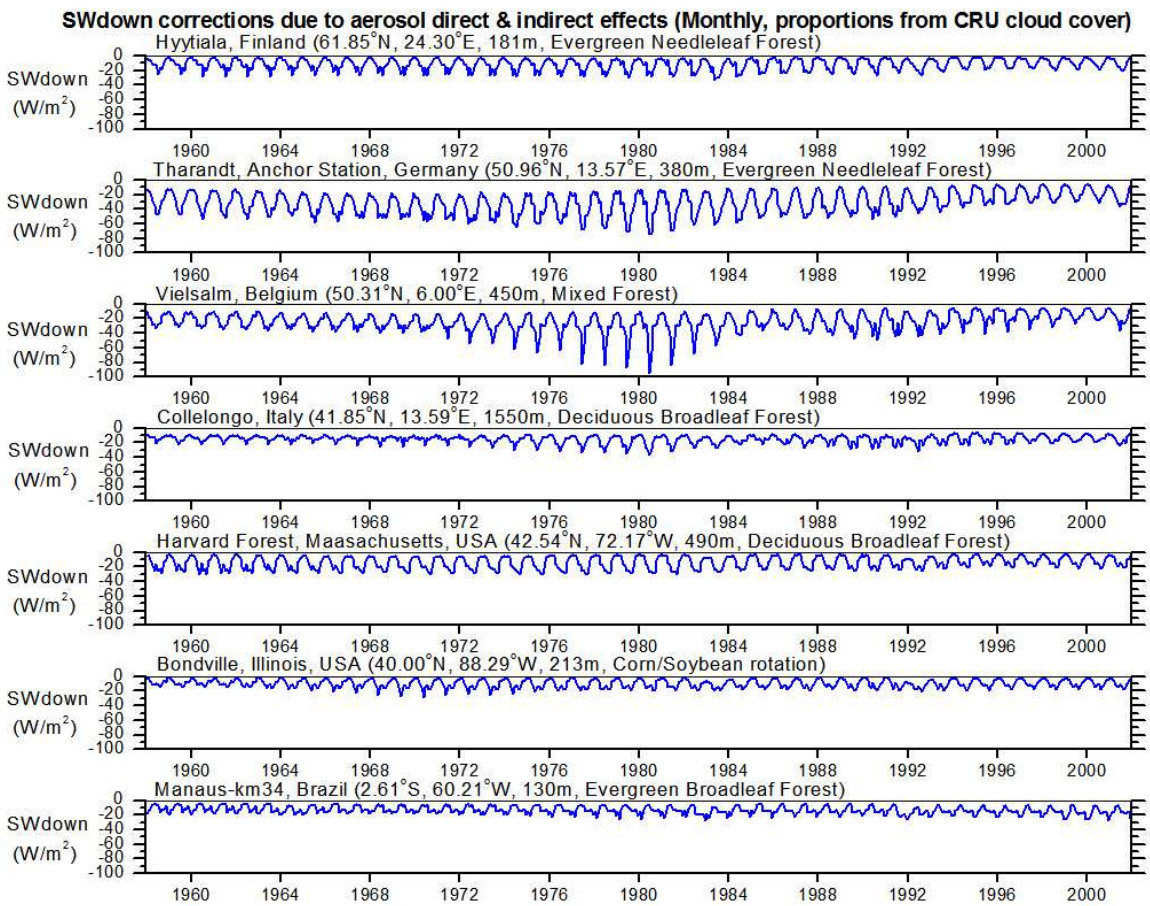

Figure 14: *Monthly average corrections of downwards short-wave radiation fluxes (SWdown) due to direct and indirect aerosol loading variations at selected FLUXNET sites for 1958-2001.*

iii) Validation

Fig. 14 illustrates corrections for the selected FLUXNET sites. This shows how corrections due to changing aerosol loading vary through time; with maximum corrections due to 1980s summer industrial aerosol production prior to extensive clean-air legislation apparent in north-central Europe (at Tharandt and Vielsalm). Spatial patterns of the radiation-flux corrections are illustrated for winter 1980 and 2000 and summer 1980 and 2000 in Fig. 15. Again the decrease in summer corrections required for Europe are apparent as are the increased corrections needed over southern Asia over the last two decades.

The corrections (always negative) were applied for non-zero time steps in *SWinterm* using:

$$SW_{WFD}(l,t) = SWintm(l,t) + SWcorr(l,month) \quad (51)$$

As for downwards long-wave fluxes (Section 2e) the WFD short-wave fluxes have been compared with the SRB version 3 SWQC product using averages from 1984-2001:

$$SW_{SRB}CalMon(l,calmonth) = \mathbf{Mean}[SW_{SRB}Mon(l,month)] \quad (52)$$

$$SW_{WFD}CalMon(l,calmonth) = \mathbf{Mean}[SW_{WFD}Mon(l,month)] \quad (53)$$

used to obtain an offset applied to data from 1958-2001:

$$SW_{WFD}SRB(l,t) = SW_{WFD}(l,t) \times \frac{SW_{SRB}CalMon(l,calmonth)}{SW_{WFD}CalMon(l,calmonth)} \quad (54)$$

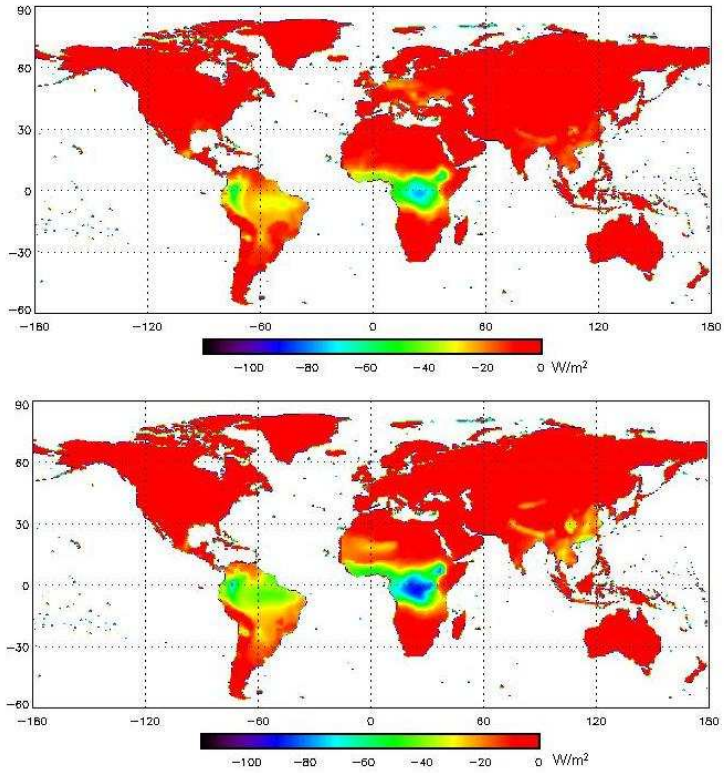

Figure 15a *Corrections to downwards short-wave radiation fluxes due to tropospheric and stratospheric aerosol loading in Top: January 1980 and Bottom: January 2000.*

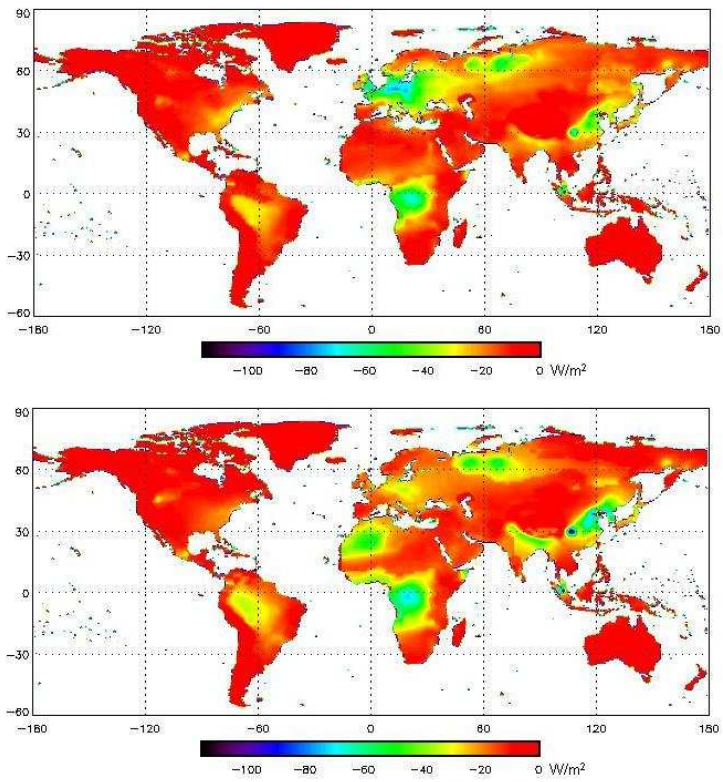

Figure 15b *Corrections to downwards short-wave radiation fluxes due to tropospheric and stratospheric aerosol loading in Top: July 1980 and Bottom: July 2000.*

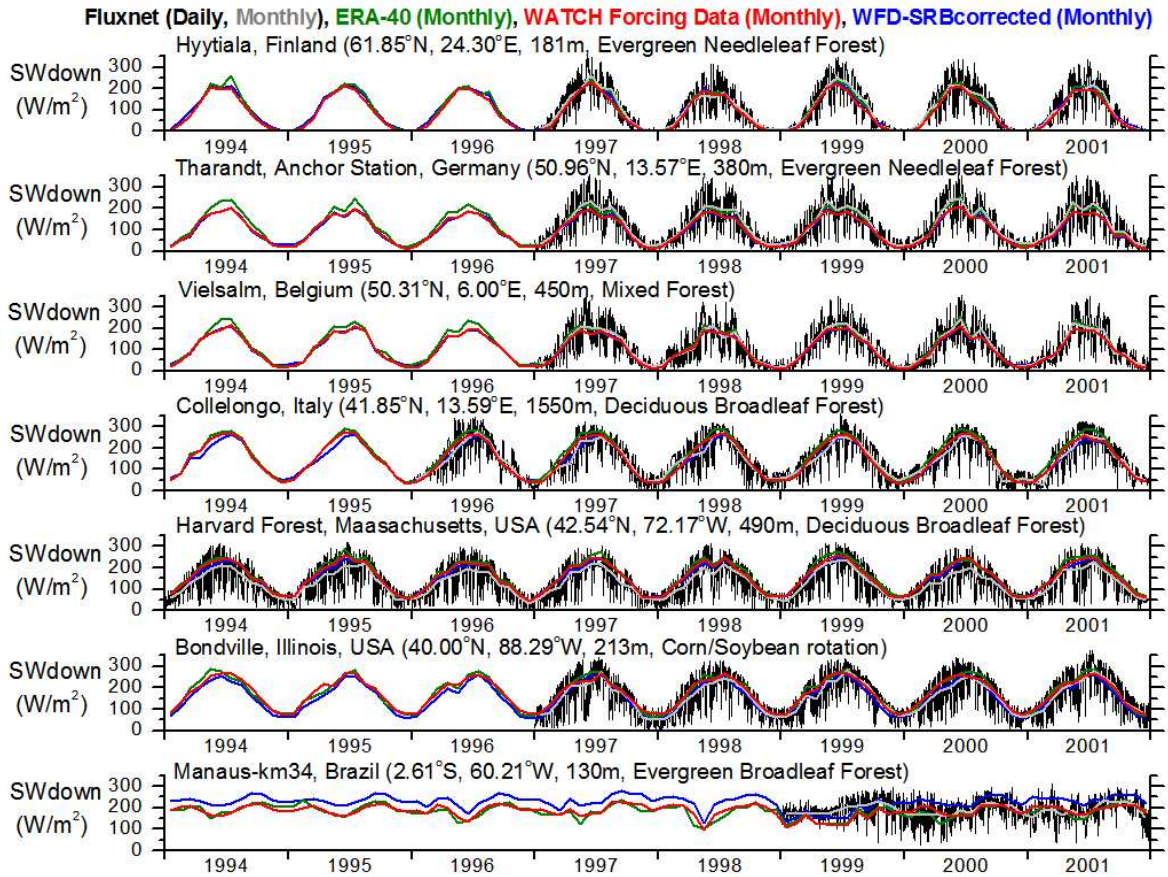

Figure 16: *Comparison of Monthly average incoming short-wave radiation flux (SWdown) from the interpolated ERA-40 data (olive), WATCH Forcing Data (red) with monthly average incoming short-wave radiation flux from SRBv3-corrected WATCH Forcing Data (blue) and with daily (black) and monthly (grey) FLUXNET data.*

Fig. 16 compares, at the selected FLUXNET sites, the monthly average interpolated ERA-40 downwards short-wave radiation flux (*SWinterp*, olive) with the WFD (SW_{WFD}, red), WFD adjusted using SRB version 3 SWQC ($SW_{WFD}SRB$, Darnell et al., 1992, blue) with the daily average FLUXNET data (black) plus the associated monthly averages (grey). SW_{WFD} and interpolated ERA-40 values agree well in most cases (except at Hyytiälä and Tharandt in the summer). Generally SW_{WFD} and the $SW_{WFD}SRB$ agree well in most places except at Manaus. At Tharandt and Vielsalm, where the biggest aerosol corrections are applied out of the selected FLUXNET sites, SW_{WFD} and $SW_{WFD}SRB$ agree very well. By comparison with the FLUXNET data at Manaus the SRB-adjustment results in downwards short-wave fluxes that are far too large. Gupta et al. (1999) attribute higher SRB short-wave fluxes at Manaus partly to insufficient accounting for aerosols from biomass burning. At the seasonal scale the SW_{WFD} and $SW_{WFD}SRB$ generally slightly underestimate the FLUXNET monthly average values in summer at Hyytiälä, Tharandt and Vielsalm. At Collelongo and Harvard Forest the FLUXNET monthly averages are slightly over-estimated by both SW_{WFD} and SRB-adjusted WFD in the spring, summer and autumn. At Bondville the FLUXNET averages are over-estimated by SW_{WFD}, but sometimes over-estimated and sometimes underestimated by $SW_{WFD}SRB$.

Fig. 17 illustrates winter- and summer-average downwards short-wave fluxes for 1984-2001. The difference between these values and that for the SRB-adjusted WFD are

shown in the bottom parts of Fig. 17a and b. Sheffield et al. (2006) found that their interpolated NCEP-NCAR reanalysis data were consistently less than SRB values worldwide on land. In contrast there are some areas where the SW_{WFD} are larger than the SRB-adjusted data (e.g. in winter: south east Asia and in summer: Greenland, part of west Africa, Oman, Pakistan and Tibet) and some areas where they are smaller (in winter and summer: especially tropical areas and in summer: much of Europe, Siberia and Alaska).

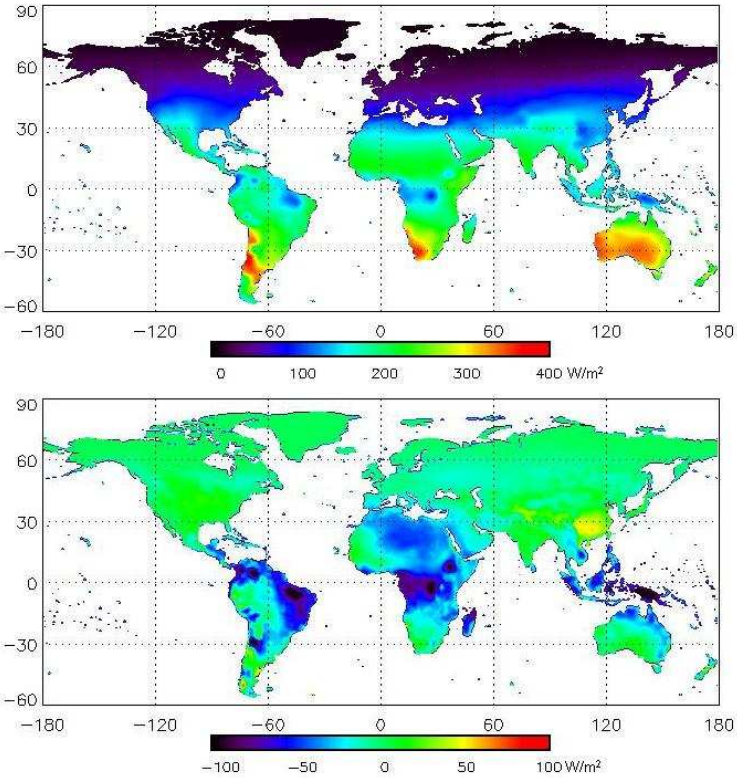

Figure 17a *Top: Average winter (DJF) downwards short-wave radiation flux in the WATCH Forcing Data 1984-2001. Bottom: Average winter downwards short-wave radiation in the WFD minus NASA SRB3-offset WFD 1984-2001.*

Part of the difference in winter especially in central Africa can be explained as related to the aerosol correction (compare Fig. 17a bottom with Fig 15a) and aerosols from burning have been identified as a cause of positive bias in SRB data in parts of Africa and South America (Gupta et al., 1999). However, the aerosol corrections applied do not explain why SW_{WFD} is higher than $SW_{WFD}SRB$ in south east Asia nor why it is lower in Indonesia. The aerosol corrections also cannot explain the higher summer SW_{WFD} compared to $SW_{WFD}SRB$ in north east Brazil nor Indonesia nor in the Sahel region of Africa (around 10°N, compare Fig 17b bottom with Fig 15b). In the case of the Sahel disparity it is possible that the explanation lies in cloud cover as well as aerosols from burning. Fig. 18 is used to support the idea that differences in cloud cover explain the disparity in the Sahel during the summer. According CRU the cloud cover (used to correct *SWinterp*) is fairly elevated across the Sahel region whereas the average summer short-wave flux in this area according to the SRBv3 SWQC data accords to much clearer-sky conditions (Fig. 18). Gupta et al., (1999) showed that locally SRB short-wave fluxes are over-estimated compared to flux tower measurements due to insufficient modelling of cloud cover.

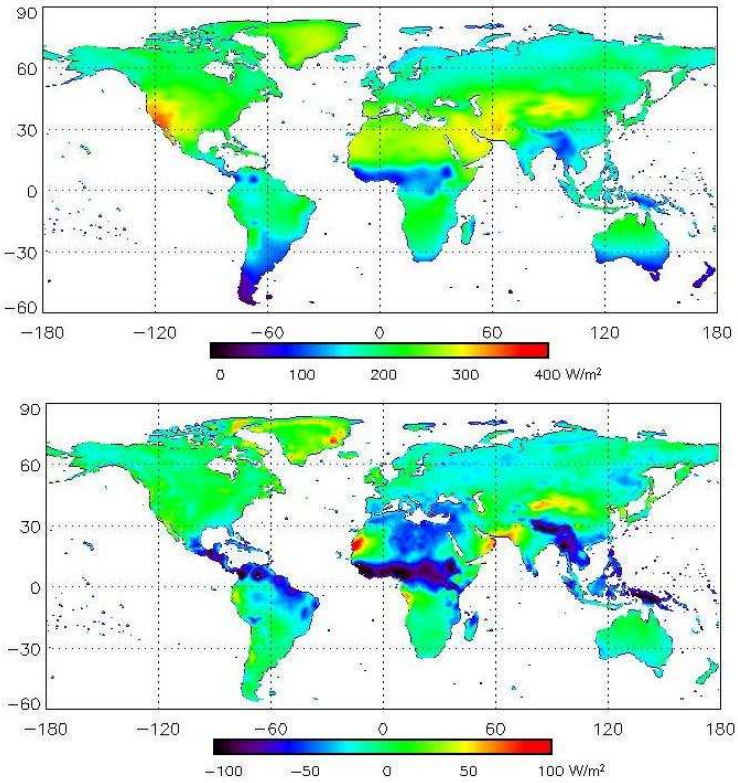

Figure 17b) *Top: Average summer (JJA) incoming short-wave radiation flux in the WATCH Forcing Data 1984-2001. Bottom: Difference between average summer incoming short-wave radiation in the WATCH Forcing Data and NASA SRB3-corrected WATCH Forcing Data 1984-2001.*

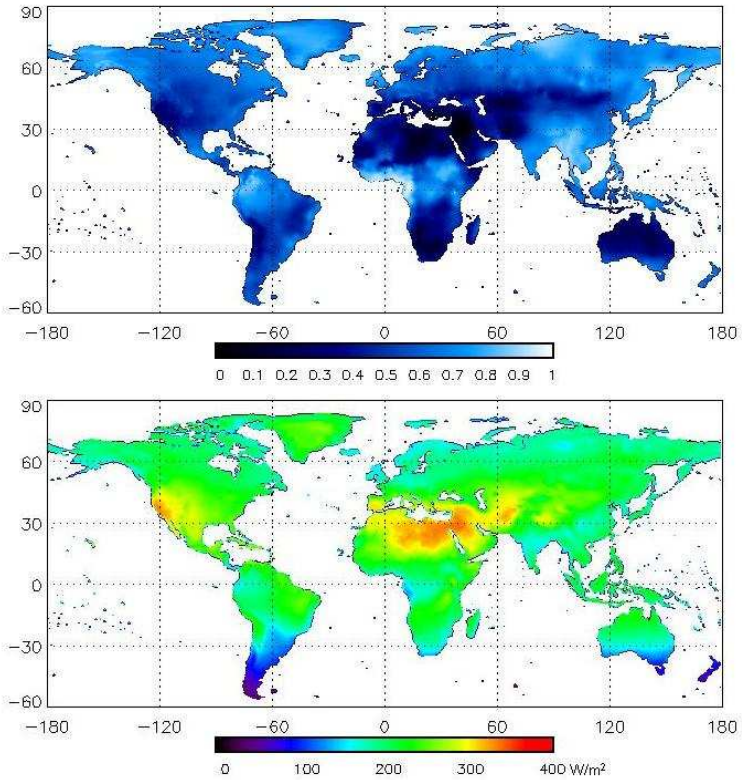

Figure 18 *Top: average summer CRU TS2.1 cloud cover (1984-2001). Bottom: Average summer (JJA) incoming short-wave radiation flux in NASA's SRB3 SWQC dataset (1984-2001).*

In summary, there are some differences between SW_{WFD} and $SW_{WFD}SRB$, but as for the long-wave data (Section 2e), not the clear-cut uni-directional biases with the FLUXNET data or satellite product to justify treating the SRB-adjusted data as superior to SW_{WFD}.

2g) Precipitation flux

i) Introduction

From the perspective of hydrological modelling within WATCH clearly the precipitation fluxes to be used in the WFD need to possess characteristics that agree with observations as closely as possible. There are important disparities between ERA-40 monthly precipitation totals and both CRU and GPCP totals especially in tropical latitudes and additionally the global water budget in ERA-40 is not closed (i.e. the excess precipitation versus evaporation over land is not matched by the deficit in precipitation versus evaporation over the ocean, Betts et al., 2003; Hagemann et al., 2005; Uppala et al., 2005). Ngo-Duc et al., (2005) corrected the precipitation totals from the interpolated NCEP-NCAR reanalysis data using CRU observations that had been degraded to one-degree resolution. Sheffield et al. (2006) added to these corrections by also correcting the number of CRU "wet days" (the number days per month with rainfall and/or snowfall) as well as correcting for precipitation gauge-undercatch via the gridded average catch ratios of Adam and Lettemaier (2003). The wet-day correction was partly necessary to remove spurious northern latitude spatial-patterns in precipitation probabilities inherent in the NCAR-NCEP reanalysis (figure 1 of Sheffield et al., 2004).

The wet-day correction adopted by Sheffield et al. (2006), utilizing the methods of Sheffield et al. (2004) involved randomly allocating, with the correct conditional probability, a particular grid cell's precipitation. When the randomly allocated state, "wet" or "dry", matched the state of the preceding day the randomly allocated precipitation rate was adopted, otherwise the precipitation value was replaced by one selected at random from the library of days of interpolated precipitation. For locations where wet days substituted for dry days and vice versa, the other variables meteorological also had to be resampled. This method allowed adjustment of the interpolated precipitation data so that the number of wet days in each grid cell matches that of the one-degree version of the CRU wet day observations. However, this approach had the effect of destroying the spatial coherence of large-scale (frontal) precipitation events (e.g. figure 7 of Sheffield et al., 2004). Consequently, Sheffield et al. (2006) explicitly state that the intended use of their forcing data is for long-term (monthly and longer) land-surface modelling precisely because of this disruption of spatial coherence. Clearly within the context of WATCH and the hydrological modelling of synoptic-scale extremes it is desirable to employ an alternative strategy for wet-day corrections.

ii) Wet-day correction

The approach used was derived after extensive discussion and experimentation between Workblock 1 and 3 and cannot be considered to be a perfect solution to the problem. However, it is considered expedient and sufficient to provide credible precipitation data for hydrological modelling at least at the sub-monthly, if not weekly or daily scale. The interpolated ERA-40 large-scale precipitation (*LSP*) and convective precipitation (*CP*):

$$PNinterp(l,t) = \mathbf{Interp}[LSP(l_{ERA},t) + CP(l_{ERA},t)] \qquad (55)$$

is used to calculate the number of wet days (i.e. following CRU meaning days with more than 1mm of rainfall plus (water-equivalent) snowfall). Compared to CRU, the number of wet days in the tropics is much larger in *PNinterp* in the winter and summer (Fig. 19). The interpolated ERA-40 data do not exhibit the spurious northern hemisphere spatial patterns of precipitation discussed by Sheffield et al. (2004).

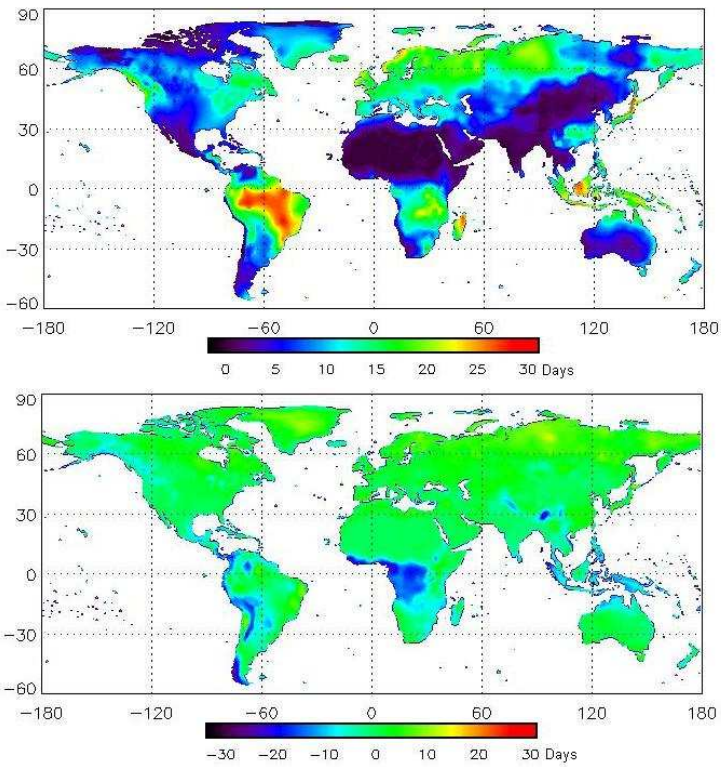

Figure 19a *Top: average number of wet days per month in winter (DJF) in CRU TS 2.1. Bottom: average number of wet days per month in winter in CRU minus wet days in interpolated ERA-40 rainfall*

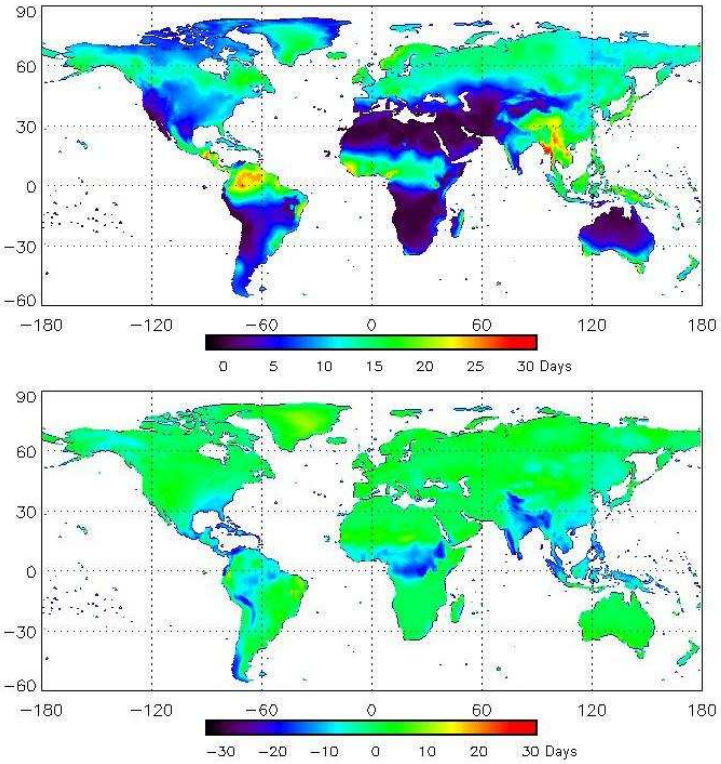

Figure 19b *Top: average number of wet days per month in summer (JJA) in CRU TS 2.1. Bottom: average number of wet days per month in summer in CRU minus wet days in interpolated ERA-40 rainfall.*

A wet day correction has been applied for locations and months where the number of wet days in *PNinterp* exceeds the number of wet days in CRU (*CRUwet*). The procedure involved repeatedly re-setting to zero, for each location and month, the day-of-the-month having the lowest precipitation rate. This was continued until the number of wet days in the month matched *CRUwet*. The method is designed to reduce the number of wet days down to the CRU observations, but without destroying the spatial coherence of widespread precipitation events (e.g. frontal rain affecting multiple half-degree grid boxes simultaneously and/or sequentially). In particular, the places and days with the lowest precipitation rates have been targeted for removal because they are least significant from the perspective of hydrological modelling (particularly with regard to floods and droughts). The procedure is designed using the assumption that the lowest precipitation rate in widespread events that include high rates of precipitation, is usually associated spatially with the edges of areas of rainfall or snowfall. For simplicity and ease of coding, in places and at times when precipitation has been removed, no attempt has been made to modify the other meteorological variables.

A deficit in monthly wet days in the interpolated precipitation compared to CRU is actually comparatively rare with, outside Greenland, small areas involved in north Siberia in winter and small areas in north east Brazil (Fig. 19). Consequently, no wet-day correction has been applied when the number of wet days in *PNinterp* is less than *CRUwet*. Addition of precipitation on selected dry days in a way that would be consistent with the hydrological modelling of sub-monthly meteorological variability would need to ensure that: a) associated variables (especially downwards short-wave flux, 2m temperature and specific humidity) are consistent with the added rain or snow, b) the added precipitation is spatially coherent across grid boxes, and c) the added precipitation is consistent with the synoptic situation (weekly-to-monthly pressure variations) as diagnosed by the GCM reanalysis. However, in areas with a deficit in wet days, but with several days of very low precipitation rates, potentially the bias-correction step (Section 2g iii) could lead to increased rates and thus increase the number of days associated with daily totals exceeding the 1mm threshold for wet day definition. This explains why in the final data there are actually exceedingly few areas with a deficit in wet days compared to CRU (Fig. 20).

iii) Bias-correction

In order to correct the total monthly precipitation in the wet-day-corrected *PNinterp*, data have been obtained from the Global Precipitation Climatology Centre (GPCC) half-degree version 4 full product (Table 2). This consists of monthly gridded precipitation totals (*GPCCPN*) from rain-gauge observations (i.e. without integration of satellite products) in a system that is very like CRU, but with a much greater number of stations particularly in 1990-2001 (compare Mitchell and Jones, 2005 and Fuchs, 2008). For some places, especially islands, represented by one or very few boxes in the CRU grid that are not covered by GPCC v4, we have employed the CRU TS2.1 precipitation totals. Following Ngo-Duc et al. (2005) and Sheffield et al. (2006) we corrected the sub-daily precipitation rates using:

$$PN_{GPCC}(l,t) = PNinterp(l,t) \times \frac{GPCCPN(l,month)}{PNinterpMonTot(l,month)} \qquad (56)$$

where *PNinterpMonTot* indicates monthly total precipitation. Next the precipitation was allocated to interim snowfall- (*SFintmGPCC*) and rainfall-rates (*RFintmGPCC*) in the proportions associated with the interpolated data:

$$SFinterp(l,t) = \mathbf{Interp}[SF(l_{ERA},t)] \quad (57)$$

using:

$$SFintmGPCC(l,t) = PN_{GPCC}(l,t) \times \frac{SFinterp(l,t)}{PNinterp(l,t)} \quad (58)$$

so that:

$$RFintmGPCC(l,t) = PN_{GPCC}(l,t) - SFintmGPCC(l,t) \quad (59)$$

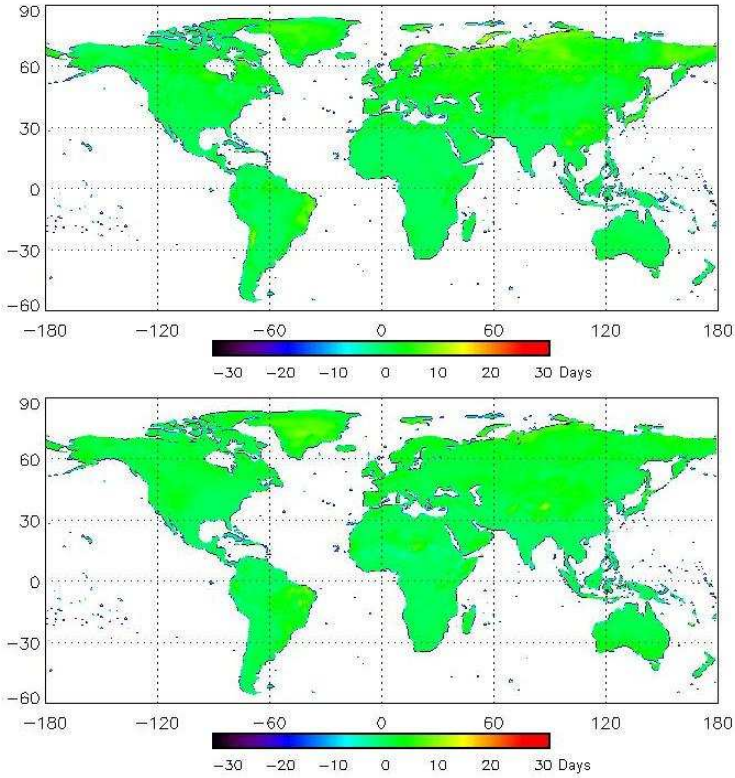

Figure 20 *Top: average number of wet days per month in winter (DJF) in CRU minus the number in* PN_{WFD}*GPCC. Bottom: average number of wet days per month in summer in CRU minus the number in* PN_{WFD}*GPCC.*

To allow comparison of the effects of the GPCC- and CRU-derived precipitation totals we repeated this exercise using the CRU precipitation totals (*CRUPN*) in place of *GPCCPN*:

$$PN_{CRU}(l,t) = PNinterp(l,t) \times \frac{CRUPN(l,month)}{PNinterpMonTot(l,month)} \quad (60)$$

so that the corresponding interim snowfall and rainfall rates are:

$$SFintmCRU(l,t) = PN_{CRU}(l,t) \times \frac{SFinterp(l,t)}{PNinterp(l,t)} \quad (61)$$

and:

$$RFintmCRU(l,t) = PN_{CRU}(l,t) - SFintmCRU(l,t) \quad (62)$$

Note that the CRU TS2.1 totals were not corrected for inhomogeneity prior to their use (cf. Österle et al., 2003).

iv) Precipitation gauge catch-correction

Sheffield et al. (2006) corrected their precipitation rates using the precipitation gauge catch ratios of Adam and Lettenmaier (2003). The "catch ratios", which allow for gauge design, wind-induced undercatch and wetting losses, provided as average calendar month values on a half-degree grid, allow a simple correction to be applied to sub-daily precipitation rates. Each catch ratio for each calendar month represents the average precipitation measured in local gauges divided by the catch-corrected precipitation (Adam and Lettenmaier, 2003).

However, only single values were provided for each month and grid box – in other words separate corrections for rainfall and snowfall were not provided. This means that in high latitude and/or high altitude grid boxes where snow is expected in winter, there is the possibility of incorrectly applying a snowfall catch ratio in years where, unusually, there is substantial rainfall. Consequently separate catch ratios have now been created for rain (*CRrain*) and snow (*CRsnow*) at every grid box. In some coastal areas and small islands, where the original half-degree catch ratio grid did not include all the CRU grid boxes, a catch ratio of unity has been assumed. Fig. 21 illustrates January and July catch ratios for rain and snow. Note that in parts of western Canada measurements of snow thickness are used in place of precipitation gauges so the catch ratio exceeds 1.0 (i.e. the snow-water equivalent rates are decreased in these areas during correction). Fig. 21 illustrates the CR ratios in January and July.

The precipitation gauge corrections were applied using:

$$RF_{WFD}GPCC(l,t) = RFintmGPCC(l,t)/CRrain(l,calmonth) \quad (63)$$

$$SF_{WFD}GPCC(l,t) = SFintmGPCC(l,t)/CRsnow(l,calmonth) \quad (64)$$

$$RF_{WFD}CRU(l,t) = RFintmCRU(l,t)/CRrain(l,calmonth) \quad (65)$$

$$SF_{WFD}CRU(l,t) = SFintmCRU(l,t)/CRsnow(l,calmonth) \quad (66)$$

Fig. 22 compares daily average FLUXNET and WFD precipitation at the selected sites. Note that since the WFD data are based on half-degree grid box averages one would not expect very close correspondence in timing or the size of extremes for particular rainfall or snowfall events. Nevertheless, at some sites (Hyytiälä, Tharandt and Harvard Forest) the agreement is remarkably good.

v) Remaining issues

The processing procedures adopted for WFD precipitation have resulted in a few remaining issues. The most serious concerns outliers in precipitation rates where in a few isolated places, especially near the boundaries of the Inter-tropical Convergence Zone exceptionally extreme precipitation rates were created. This problem occurs when, in places with fewer wet days than in CRU (since wet days were not created artificially – Section 2ii), substantially higher monthly totals in GPCC compared to ERA-40 results in implausibly high precipitation rates following bias-correction. We have addressed this issue by using a locally-

based threshold used to clip extreme rates. Thus the log-normal probability of precipitation rates was established in 1980 and 1981. Then, if in a particular time interval the precipitation rate exceeded the 99.999% log-normal probability for that location it was re-set at the threshold level. Ideally more years could have been used to establish the probability function, but time pressures within WATCH prevented this.

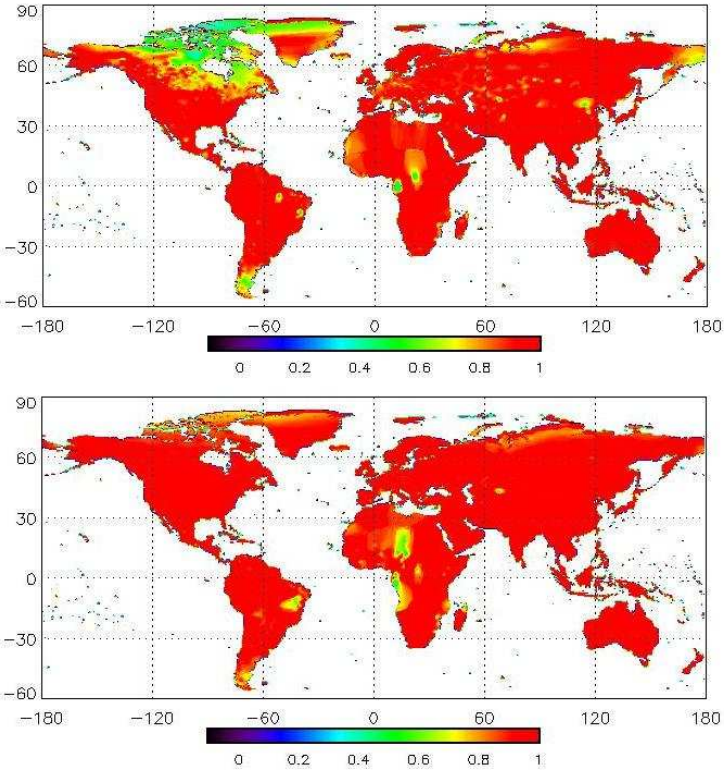

Figure 21a *Precipitation gauge catch ratios for rain in Top: January and Bottom: July.*

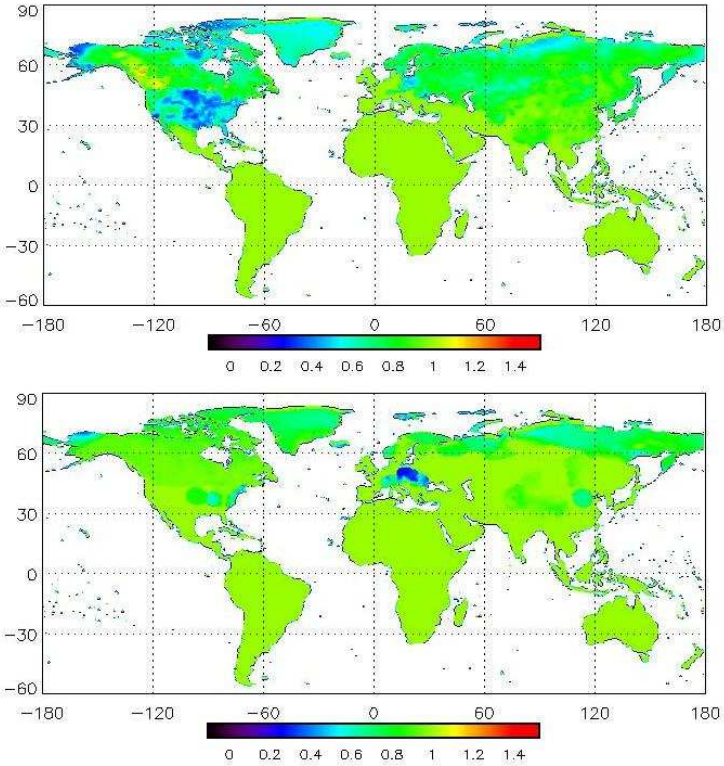

Figure 21b *Precipitation gauge catch ratios for snow in Top: January and Bottom: July.*

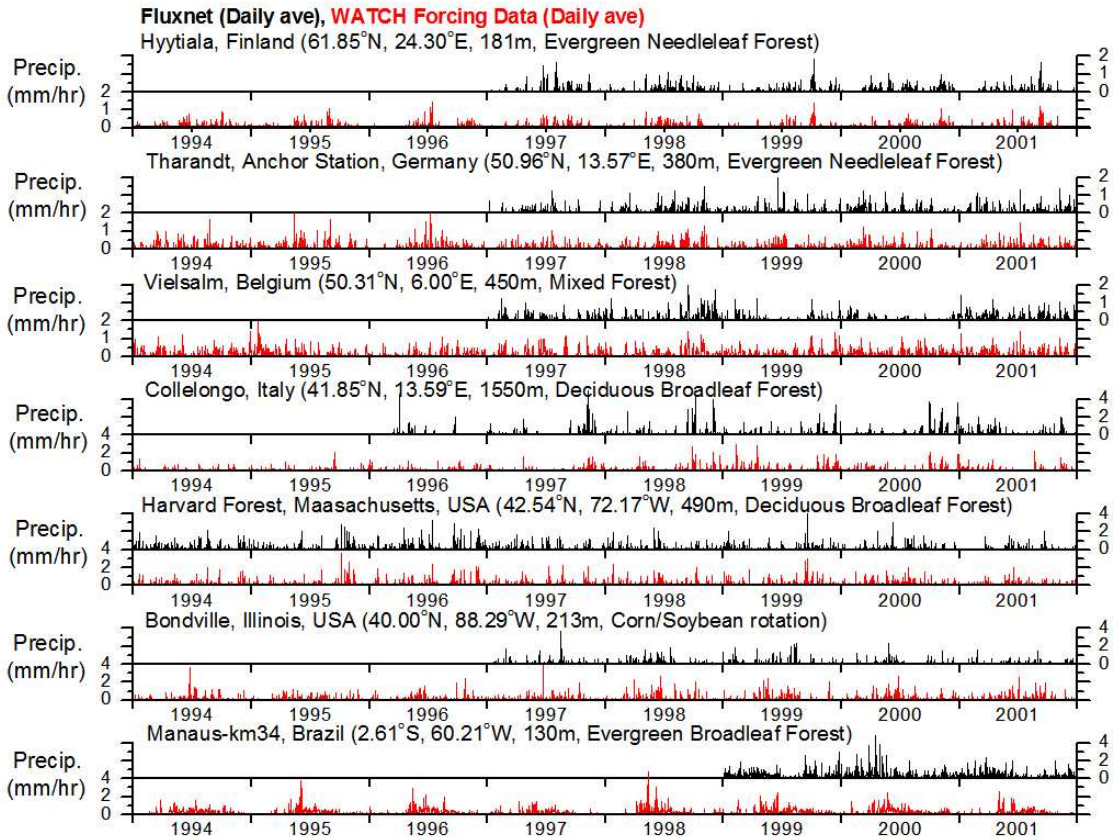

Figure 22: *Comparison of daily average rate of precipitation (rainfall plus snowfall) from the WATCH Forcing Data (red) with daily average rate of precipitation in the Fluxnet data (black).*

ERA-40 includes, in a few places and a few months, precipitation rates that are just above zero at all time steps apart from times of "natural" precipitation. Unfortunately the monthly bias-correction step has very rarely had the effect of increasing these background rates to a level where the final data imply a spurious constant "drizzle" through the month. In semi-arid regions such precipitation is clearly not consistent with the local climatic conditions. From the point-of-view of hydrological modelling this low-level background is not significant. Again time pressures prevented adoption of a viable solution to this problem.

Although gauge-correction was applied to the WFD precipitation data, this did not include any allowance for orographic effects that can bias gauge readings. Such effects can be very substantial in some places and corrections have been calculated (Adam et al., 2006). However, adoption of gauge corrections for orography depends on detailed treatment of the particular datasets involved and require local streamflow data and modelling of evapo-transpiration. This work was beyond the scope of this data generation exercise, but hydrologically it is clear that orographic effects will have been underestimated in the WFD precipitation data (Adam et al., 2006).

Fig. 23 compares the final average winter and summer precipitation based on the GPCC-totals, and the CRU-totals. It is clear that in the great majority of areas there is no difference, but in north east India there are substantial divergences between the GPCC and CRU totals. On balance, given the much greater numbers of stations (Fuchs pers. comm., 2008, Fuchs, 2008) we favour the data derived using the GPCC values.

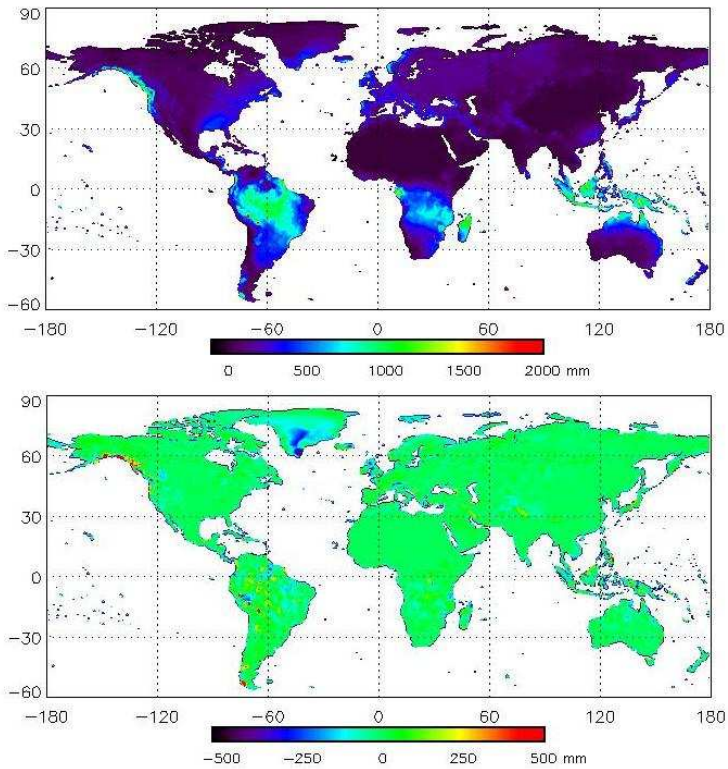

Figure 23a *Top: winter (DJF) average precipitation totals (rainfall plus snowfall) for the WFD corrected using GPCC v4 full product totals. Bottom: as for Top, but minus winter average rate of precipitation for the WFD corrected using GPCC v4 totals minus WFD corrected using CRU TS2.1 totals.*

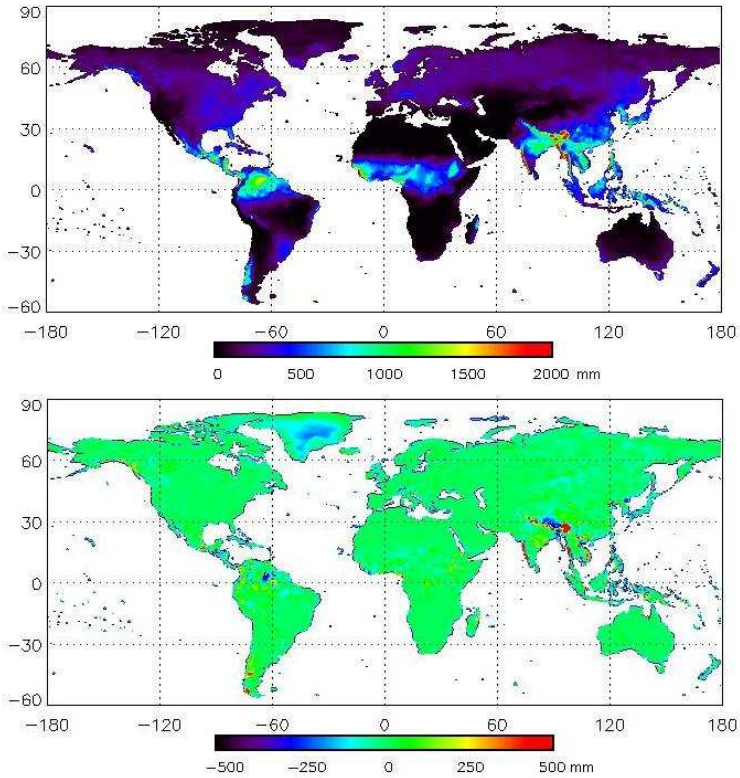

Figure 23b *Top: Summer (JJA) average precipitation totals (rainfall plus snowfall) for the WFD corrected using GPCC v4 full product totals. Bottom: as for Top, but minus summer average rate of precipitation for the WFD corrected using GPCC v4 totals minus WFD corrected using CRU TS2.1 totals.*

3) Conclusion

The data set provided here has been designed to allow half-degree hydrological modelling. This required adjustments to the ERA-40 pioneered in previous forcing datasets (Ngo-Duc et al., 2005; Sheffield et al., 2006) and adding the use of new data (GPCC v4 for precipitation, varying atmospheric aerosol loading effects, separated catch ratios). Comparison with FLUXNET data demonstrates a close correspondence between field-measured and these adjusted reanalysis data for all variables.

Acknowledgements

Our thanks to the following for permission to illustrate flux tower data: Steven Wofsy; Alessandro Araújo; Celso von Randow; Bart Kruijt; Thomas Grünwald; Timo Vesala and Giorgio Matteucci. Nick Reynard (Reading) suggested obtaining separate catch ratios for rain and snow. Tobias Stacke (MPI-Hamburg) generously helped with the processing of the precipitation data and checking the temperature data. GPW was supported by the Joint DECC and Defra Integrated Climate Programme – DECC/Defra (GA01101).

References

Adam, J.C., Clark, E.A. and Lettenmaier, D.P., 2006. Correction of global precipitation for orographic effects. *J. Clim.* **19**, 15-38.

Adam, J.C. and Lettenmaier, D.P., 2003. Adjustment of global gridded precipitation for systematic bias. *J. Geophys. Res.*, **108**, D9, 4257, doi:10.1029/2002JD002499, 2003.

Araújo, A.C., Nobre, A.D., Kruijt, B., Elbers, J.A., Dallarosa, R., Stefani, P., von Randow, C., Manzi, A.O., Culf, A.D., Gash, J.H.C., Valentini, R., and Kabat, P., 2002. Compartive measurements of carbon dioxide fluxes from two nearby towers in a central Amazonian rainforest. *J. Geophys. Res.* **107**, D20, 8090, doi:10.1029/2001JD000676.

Bellouin, N., Boucher, O., Haywood, J., Johnson, C., Jones, A., Rae, J. and Woodward, S., 2007. Improved representation of aerosols for HadGEM2, Hadley Centre Tech. Note 73, Met Office, Exeter, UK, 43pp. (available at: http://www.metoffice.gov.uk/research/publications/HCTN/index.html.)

Betts, A.K. and Beljaars, A.C.M., 2003. ECMWF ISLSCP-II near-surface dataset from ERA-40. *ERA-40 Project Rep. Ser. no. 8.* ECMWF (available at: www.ecmwf.int/publications/library/do/reference/list/192).

Brohan P., Kennedy, J.J., Harris, I., Tett, S.F.B. and Jones P.D., 2006. Uncertainty in regional and global observed temperature changes: a new data set from 1850. *J. Geophys. Res.* **111**, D12106, doi:10.1029/2005JD006548.

Buck, A.L., 1981. New equations for computing vapour pressure and enhancement factor. *J. App. Meteo.* **20**, 1527-1532.

Collins, W.J., Bellouin, N., Doutriaux-Boucher, M., Gedney, N., Hinton, T., Jones, C.D., Liddicoat, S., Martin, G., O'Connor, F., Rae, J., Senior, C., Totterdell, I., Woodward, S., Reichler, T., and Kim, J., 2007. Evaluation of HadGEM2 model, Hadley Centre Tech. Note 74, Met Office, Exeter, UK, 47 pp (available at: http://www.metoffice.gov.uk/research/publications/HCTN/index.html).

Cox, C. and Munk, W., 1954. Statistics of the sea surface derived from sun glitter. *J. Mar. Res.* **13**, 198-227.

Darnell, W.L., Staylor, W.F., Gupta, S.K., Ritchey, N.A. and Wilber, A.C., 1992. Seasonal variation of surface radiation budget derived from international satellite cloud climatology project C1 data. *J. Geophy. Res.* **97**, D14, 15,741-15,760.

Dessler, A.E., Zhang, Z. and Yang, P., 2008. Water-vapor climate feedback inferred from climate fluctuations 2003-2008. *Geophys. Res. Lett.* **35**, L20704, doi:10.1029/2008GL035333, 2008.

Dubovik, O., Holben, B., Eck, T.F., Smirnov, A., Kaufman, Y.J., King, M.D., Tanre, D. and Slutsker, I., 2002. Variability of absorption and optical properties of key aerosol types observed in worldwide locations. *J. Atmos. Sci.* **59**, 590-608.

Fuchs, T., 2008. GPCC Annual report for year 2008. Development of the GPCC data base and analysis products (available from reports and publications section of the GPCC homepage - gpcc.dwd.de).

Göckede, M., Foken, T., Aubinet, M., Banza, J., Bernhofer, C., Bonneford, J.M., Brunet, Y., Carrara, A., Clement, R., Dellwik, E., Elbers, J., Eugster, W., Fuher, J., Granier, A., Grünwald, T., Heinesch, B., Janssens, I.A., Knohl, A., Koeble, R., Laurila, T., Longdoz, B., Manca, G., Marek, M., Markkanen, T., Mateus, J., Matteucci, G., Mauder, M., Migliavacca, M., Minerbi, S., Moncrieff, J., Montagnani, L., Moors, E., Ourcival, J-M., Papale, D., Perira, J., Pilegaard, K., Pita, G., Rambal, S., Rebmann, C., Rodrigues, A., Rotenberg, E., Sanz, M.J., Sedlak, P., Seufert, G., Siebicke, G., Soussana, J.F., Valentini, R., Vesala, T., Verbeeck, H., and Yakir, D., 2008. Quality control of CarboEurope flux data – Part 1: coupling footprint analyses with flux data quality assessment to evaluate sites in forest ecosystems. *Biogeosci.* **5**, 433-450.

Grünwald, T., and Bernhofer, C., 2007. A decade of carbon, water and energy flux measurements of an old spruce forest at the Anchor Station Tharandt. *Tellus* **59B**, 387-396.

Gupta, S.K., 1989. A parameterization for long-wave surface radiation from Sun-synchronous satellite data. *J. Clim.* **2**, 305-320.

Gupta, S.K., Darnell, W.L. and Wilber, A.C., 1992. A parameterization for longwave surface radiation from radiation from satellite data: recent improvements. *J. App. Meteo.* **31**, 1361-1367.

Gupta, S.K., Ritchey, N.A., Wilber, A.C. and Whitlock, C.H., 1999. A climatology of surface radiation budget derived from satellite data. *J. Clim.* **12**, 2691-2710.

Hagemann, S., Arpe, K. and Bengtsson, L., 2005. Validation of the hydrological cycle of ERA-40. *ERA-40 Project Rep. Ser. no. 24.* ECMWF (available at: www.ecmwf.int/publications/library/do/reference/list/192).

Key, J. R. & Schweiger, A. J., 1998. Tools for atmospheric radiative transfer: STREAMER and FLUXNET. *Comput. Geosci.* **24**, 443-451.

Martin, G. M., Ringer, M.A. Pope, V.A., Jones, A., Dearden, C., and Hinton, T.J., 2006. The physical properties of the atmosphere in the new Hadley Centre Global Environmental Model, HadGEM1. Part 1: Model description and global climatology, *J. Clim.* **19**, 1274-1301.

Meyers, T.P. and Hollinger, S.E., 2004. An assessment of storage terms in the surface energy balance of maize and soybean. *Agri. Forest Meteo.* **125**, 105-115.

Mitchell, T.D. and Jones, P.D., 2005. An improved method of constructing a database of monthly climate observations and associated high-resolution grids. *Int. J. Clim.* **25**, 693-712.

Myhre, G., Berglen, T.F., Myhre, C.E.L., Isaksen, I.S.A., 2004. The radiative effect of the anthropogenic influence on the stratospheric sulfate aerosol layer. *Tellus*, **56B**, 294-299.

New, M., Hulme, M., and Jones, P., 1999. Representing twentieth century space-time climate variability, Part I: Development of a 1961-90 mean monthly terrestrial climatology. *J Clim.* **12**, 829-856.

New, M., Hulme, M., and Jones, P., 2000. Representing twentieth century space-time climate variability, Part II: Development of 1901-96 monthly grids of terrestrial surface climate. *J Clim.* **12**, 829-856.

Ngo-Duc, T., Polcher, J. and Laval., K., 2005. A 53-year forcing data set for land surface models. *J. Geophys. Res.* **110**, D06116, doi:10.1029/2004/D005434.

Österle, H., Gertengarbe, F-W., Werner, P.C., 2003. Homogenisierung und Aktualisierung des Klimadatensatzes der Climate Research Unit der University of East Anglia, Norwich. *Terra Nostra* **6**, 326-329.

Persson T., Van Oene H., Harrison A.F., Karlsson P., Bauer G., Cenry J., Coûteaux M.-M., Dambrine E., Högberg P., Kjøller A. Matteucci G., Rubedeck A., Schulze E.-D., Paces T., 2000. Experimental sites in the NYPHYS/CANIF project. In: *Carbon and Nitrogen Cycling in European forest Ecosystems*, Schulze E.-D. (Ed.), *Ecological Studies* **142**, Springer Verlag, Heidelberg, 14-48.

Peterson, T.C., and Easterling, D.R., 1994. Creation of homogeneous composite climatological reference series. *Int. J. Clim.* **14**, 671-679.

Peterson, T.C., Easterling, D.R., Karl, T.R., Groisman, P., Nicholls, N., Plummer, N., Torok, S., Auer, I., Boehm, R., Gullett, D., Vincent, L., Heino, R., Tuomenvirta, H., Mestre, O., Szentimrey, T., Salinger, J., Førland, E.J., Hanssen-Bauer, I., Alexandersson, H., Jones, P., and Parker, D., 1998. Homogeneity adjustments of *in situ* atmospheric climate data: a review. *Int. J. Clim.* **18**, 1493-1517.

Pitman, A.J. and Perkins, S.E. 2009. Global and regional comparison of daily 2-m and 100-h Pa maximum and minimum temperatures in three global reanalyses. *J. Clim.* **22**, 4667-4681.

Rudolf, B. and Schneider, U., 2005. Calculation of gridded precipitation data for the global land-surface using in-situ gauge observations. *Proc. 2nd Workshop Int. Precip. Work. Gp* (available at: reports and publications section of the GPCC homepage - gpcc.dwd.de).

Sato, M., Hansen, J.E., McCormick, M.P., and Pollack, J.B., 1993. Stratospheric aerosol optical depth, 1850-1990. *J. Geophys. Res.* **98**, 22987-22994.

Schneider, U., Fuchs, T., Meyer-Christoffer, A. and Rudolf, B. 2008. Global precipitation analysis products of the GPCC (available from reports and publications section of the GPCC homepage - gpcc.dwd.de).

Sheffield, J., Goteti, G. and Wood, E.F., 2006. Development of a high-resolution global dataset of meteorological forcings for land surface modeling. *J. Clim.* **19**, 3088-3111.

Sheffield, J., Ziegler, A.D. and Wood, E.F., 2004. Correction of the high-latitude rain day anomaly in the NCEP-NCAR reanalysis for land surface hydrological modeling. *J. Clim.* **17**, 3814-3828.

Suni, T., Rinne, J., Reissell, A., Altimir, N., Keronen, P., Rannik, Ü., Maso, D.M., Kulmala, M., and Vesala, T., 2003. Long-term measurements of surface fluxes above a Scots pine forest in Hyytiälä, southern Finland, 1996-2001. *Boreal Env. Res.* **8**, 287-301.

Uppala, S.M., Kållberg, P.W., Simmons, A.J., Andrae, U., Da Costa Bechtold, V., Fiorino, M., Gibson, J.K., Haseler, J., Hernandez, A., Kelly, G.A., Li, X., Onogi, K., Saarinen, S., Sokka, N., Allan, R.P., Andersson, Arpe, K., Balmaseda, M.A., Beljaars, A.C.M., Van de Berg, L., Bidlot, J., Bormann, N., Caires, S., Chevallier, F., Dethof, A., Dragosavac, M., Fisher, M., Fuentes, M., Hagemann, Holm, E., Hoskins, B.J., Isaksen, L., Janssen, P.A.E.M., Jenne, R., McNally, A.P., Mahfouf, J-F., Morcrette, J-J., Rayner, N.A., Saunders, R.W., Simon, P., Sterl, A., Trenberth, K.E., Untch, A., Vasiljevic, D., Viterbo, P. and Woollen, J., 2005. The ERA-40 re-analysis. *Quart. J. Meteo. Soc.* **131**, 2961-3012.

Urbanski, S., Barford, C., Wofsy, S., Kucharik, C., Pyle, E., Budney, J., McKain, K., Fitzjarrald, D., Czikowsky, M., and Munger, J.W., 2007. Factors controlling CO_2 exchange on timescales from hourly to decadal at Harvard Forest. *J. Geophys. Res.* **112**, G02020, doi:10.1029/2006JG000293.

Wexler, A., 1976. Vapour pressure formulation for water in the range 0° to 100 ^oC – a revision. *J. Res. Natl. Bur. Stand.* **80A**, 775p.

Wexler, A., 1977. Vapour pressure formulation for ice. *J. Res. Natl., Bur. Stand.* **81A**, 5-20.
Wilber, A.C., Smith, G.L., Gupta, S.K. and Stackhouse, P.W., 2006. Annual cycles of surface shortwave radiative fluxes. *J. Clim.* **19**, 535-547.
Wild, M., Grieser, J. and Schär, C., 2008. Combined surface solar brightening and increasing greenhouse effect support recent intensification of the global land-based hydrological cycle. *Geophys. Res. Lett.* **35**, L17706, doi:10.1029/2008GL034842.
Willett, K.M., Gillett, N.P., Jones, P.D., and Thorne, P.W., 2007. Attribution of observed surface humidity changes to human influence. *Nature* **449**, 710-713.